

NASA Contractor Report 3073

NASA
CR
3073
c.1

LOAN COPY: RETURN TO
AFWL TECHNICAL LIBRARY
KIRTLAND AFB, N. M.



Investigation of Aircraft Landing in Variable Wind Fields

Walter Frost and Kapuluru Ravikumar Reddy

CONTRACT NAS8-29584
DECEMBER 1978

NASA



NASA Contractor Report 3073

Investigation of Aircraft Landing in Variable Wind Fields

Walter Frost and Kapuluru Ravikumar Reddy
The University of Tennessee Space Institute
Tullahoma, Tennessee

Prepared for
George C. Marshall Space Flight Center
under Contract NAS8-29584



National Aeronautics
and Space Administration

**Scientific and Technical
Information Office**

1978

AUTHORS' ACKNOWLEDGMENTS

The work reported herein was supported by the National Aeronautics and Space Administration, Marshall Space Flight Center, Space Sciences Laboratory, Atmospheric Sciences Division , under contract number NAS8-29584.

The authors are indebted to Mr. John H. Enders of the Aviation Safety Technology Branch, Office of Aeronautics and Space Technology (OAST), NASA Headquarters, Washington, D. C., for his support of this research. Special thanks also go to Dr. G. H. Fichtl and Mr. Dennis Camp of the Marshall Space Flight Center who were the scientific monitors of the program.

TABLE OF CONTENTS

CHAPTER	PAGE
I. INTRODUCTION.	1
II. AIRCRAFT LANDING MODEL.	6
1. Equations of Motion	6
2. Incorporation of Wind Shear	11
III. MATHEMATICAL MODELS FOR VARIABLE WIND FIELDS.	15
1. Atmospheric Flow Over a Homogeneous Terrain	15
2. Atmospheric Flow Over Buildings	15
3. Atmospheric Flow Associated with Thunderstorm Gust Fronts	25
IV. AUTOMATIC CONTROL SYSTEM.	29
1. Mode Selector	33
2. Altitude Hold Mode.	36
3. Capture Mode.	38
4. Glide-Slope Tracking Mode	40
5. Flare Mode.	42
6. Calculation of the Feed-Back Controls	46
V. RESULTS AND DISCUSSION.	51
VI. CONCLUSIONS	76
BIBLIOGRAPHY.	77
APPENDIX.	80

LIST OF FIGURES

FIGURE	PAGE
1. Relationship between the various forces acting on an aircraft [12].	7
2. Logarithmic wind profile	16
3. Definition of flow zones near a sharp-edged block [22]	18
4. Description of flow region considered for a block building [22].	19
5. Description of flow region considered for a long, wide building [23].	20
6. Vorticity contour [22]	21
7. Streamline patterns [22]	22
8. Velocity profiles over an obstruction on the surface [22].	23
9. Velocity profiles over a step geometry long, wide building [23].	24
10. Overall block diagram of control system.	31
11. Automatic landing geometry using ILS	34
12. Mode control logic	35
13. Altitude hold mode	37
14. Glide slope capture mode	39
15. Glide slope tracking mode.	41
16. Flare mode	44
17. Feedback loop-thrust	47
18. Feedback loop-elevator angle	49
19. Fixed control landing over a block building.	52
20. Fixed control landing over a step.	53

FIGURE	PAGE
21. Fixed control landing in the atmospheric boundary layer.	55
22. Fixed control landing in thunderstorm gust front	56
23. Wind distribution over a block building along the flight path	57
24. Wind distribution over a long; wide building along the flight path.	58
25. Wind distribution in the thunderstorm gust front along the flight path.	59
26. Automatic landing in atmospheric boundary layer.	60
27. Automatic landing over block building.	61
28. Automatic landing over a long, wide building	62
29. Automatic landing in the flow associated with thunderstorm gust front.	63
30. Controls required for landing over a block building.	65
31. Controls required for landing over a step.	66
32. Controls required for automatic landing in thunderstorm gust front	67
33. DHC-6 landing through atmospheric flow over a block building	68
34. Automatic landing reference trajectory	70

NOMENCLATURE

C_D	Drag coefficient, $D/(1/2)\rho V^2 S$
C_L	Lift coefficient, $L/(1/2)\rho V^2 S$
C_m	Pitching-moment coefficient, $M/(1/2)\rho V^2 S \bar{c}$
\bar{c}	Wing mean aerodynamic chord, m
$c_1, c_2 \dots c_y$	Constants
D	Magnitude of aerodynamic drag, N
F_T	Magnitude of thrust, N
$G(s)$	Filter transfer function
g	Magnitude of acceleration due to gravity, 9.8 m/sec^2
h	Altitude of aircraft measured from ground, m
h_r	Reference altitude, m
h_f	Initiation altitude of the feedback control law in the flare, m
h_{ramp}	Altitude at which the predictive pitch ramp command begins, m
h_{step}	Altitude at which the predictive pitch step command begins, m
ILS	Instrument Landing System, standard radio guidance installed at major airports
I_{yy}	Aircraft moment of inertia around y-axis, kg-m^2
K	Filter gain constants
L	Magnitude of aerodynamic lift force, N
L'	Vertical extent of major vertical updraft relative to the flight path
\hat{L}	Monin-Obukhov stability length
m	Airplane weight, N

q	Pitch angular velocity, radians/sec
S	Wing reference area, m ²
s	Laplace transform operator
T	Sampling time interval, sec
u _*	Friction velocity given by $u_* = \sqrt{\frac{\tau_0}{\rho}}$
V	Magnitude of aircraft velocity with respect to ground, m/sec
V _a	Magnitude of airspeed, m/sec
W _x	Magnitude of x-component of wind speed in earth axis, m/sec
W _z	Magnitude of z-component of wind speed in earth axis, m/sec
X	Horizontal coordinate, m
Z	Vertical coordinate, m
z	Z-transform operator
α	Angle of attack, radians
γ	Flight path angle, radians
γ _{ILS}	ILS glide path angle, radians
δ _e	Elevator deflection, radians
ε	Glide slope error angle, radians
θ	Pitch angle, radians
ρ	Air density, g/m ³
τ	Filter constant
τ ₁	Filter constant
τ ₀	Surface shear stress
→	Designates vector
([•])	Time derivative

CHAPTER I

INTRODUCTION

Wind is an important consideration in the analysis of airplane flight in the atmospheric boundary layer, both because of short-scale gusts or turbulence and because of large-scale variations of the mean wind. In the planetary boundary layer the mean wind decays toward the ground and has considerable horizontal variations due to irregularities in terrain. Thus, both spatial and temporal variations occur in near surface winds encountered along ascending and descending flight paths.

Previous analyses of airplane motion that have been carried out [1, 2, 3] consider, in general, only constant winds and thus neglect the effects of wind shear. This report, however, investigates the influence of variable mean wind fields and discrete gusts on the dynamics of aircraft during terminal flight operations. Mathematical models of the winds are introduced into the equations of aircraft motion, both with fixed and automatic controls; computer solutions of the resulting motion are carried out.

As an aircraft descends on its glide slope, a sudden change in horizontal wind or vertical wind, or both, will instantaneously affect the velocity of the aircraft relative to the air mass. If the shear is such that the relative velocity of the aircraft increases, the lift force will increase and the aircraft will tend to rise above the glide slope. If the shear causes a sudden decrease in the relative

velocity, the aircraft will respond by falling below the glide slope, and a hazardous condition may result.

Several reports have been published which link short and long touchdowns to a sudden wind shear occurrence during final approach [4, 5, 6, 7]. Recent accident reports also have found wind shear to be at least a contributing cause for several accidents [8, 9]. In addition, it is believed that wind has been responsible for many other accidents, though it remained undetected at the time [10, 11]. The problem of quantitatively defining the effect of shear of given magnitude on an aircraft during descent has not been completely resolved. Noteworthy studies that have investigated wind shear and/or turbulence during landing include References 3, 6, 7, and 10 through 14.

Although a very complete development of the system of equations governing airplane motion is available [1, 2], most analyses reported to date reduce the equations to those for a constant wind or employ a linearized model which requires the assumption of a uniform wind field and is not applicable for non-uniform winds.

Ramifications of the airplane motion due to the effects of temporally and spatially varying mean winds are studied in this report. Analyses of flight paths through changing mean wind fields reported in the literature are primarily two-dimensional and deal only with vertically varying horizontal winds (i.e., having a component parallel to the flat earth only).

Etkin [1] has a very complete development of the general equations of unsteady motion. Normally, the wind components of velocity are not included in the equations since it is assumed that

no wind is present. Luers and Reeves [7] developed a system of equations in two dimensions which incorporate only horizontal wind. Later in this report, a general form for the two-dimensional equations of motion is developed. This accounts for both vertical and horizontal mean wind components with both time and spatial variations.

Using this later set of equations, analyses both with fixed and automatic feedback control were carried out. In the fixed control simulation, the aircraft is trimmed at an altitude of 91 m and on a glide slope of -2.7 degrees. The corresponding throttle setting and elevator angle setting are then fixed for the remainder of the landing. These fixed control landing simulations were carried out for several different wind fields and the deviations in the glide slope and touchdown points are compared. In the cases with high wind shear, the deviations are very large and in some cases the aircraft trajectories with fixed controls are not realistic.

To overcome this difficulty an automatic control system was developed for the same two-dimensional system of equations. Every phase of the flight of an aircraft can be regarded as the accomplishment of a set task, i.e., flight on a specified trajectory. That trajectory may simply be a straight horizontal line traversed at constant speed or it may be a turn, a transition from one symmetric flight path to another. All of these situations are characterized by two common features, namely, the presence of a desired state and the departures from it, designated as errors. These errors are, of course, a consequence of the unsteady nature of the environment.

The correction of errors requires a method of measuring the error or the desired state. Some of the state information needed (i.e., air-speed, altitude, rate-of-climb, heading, etc.) is measured by standard flight instrumentation. This information is not generally sufficient, however, when both guidance and altitude stabilization are considered. For this case, the state information needed may include [1, 16] position and velocity vectors relative to a suitable reference frame, vehicle altitude, aerodynamic angles, etc. A wide variety of devices are used to measure these and other variables, and range from pitot-static tubes to sophisticated inertial-guidance platforms. Gyroscopes, accelerometers, magnetic and gyrocompasses, angle-of-attack and sideslip vanes, and other devices, all find applications as sensors. The most common form of output is an electrical signal, but fluidic devices [17] are receiving increased attention.

In this study we assume that the desired variable can be measured independently and linearly, which is of course, an idealization. Since every sensing device, together with its associated transducer and amplifier, is itself a dynamic system with characteristic frequency response, noise, nonlinearity and cross-coupling, these attributes cannot be ignored in the final design of real systems, although one can usefully do so in preliminary work [1].

In the automatic control simulation, the aircraft is trimmed initially at an altitude of 91 m on a straight horizontal line trajectory and is automatically controlled by actuation of thrust and elevator angle. In this first phase the aircraft remains in an altitude hold mode until it intersects the Instrument Landing System

(ILS) guidance beam. It then switches to the glide-slope capture mode which actuates the thrust and elevator controls so as to capture the -2.7 degree glide path specified by the ILS guidance beam. As soon as the specified glide path is captured, the third phase, glide-slope tracking mode, becomes effective. In this mode the controls are actuated such that the aircraft remains on the glide path. At an altitude of approximately 18 m, flare initiation altitude along with other necessary parameters are calculated to begin the flare mode. The flare mode is switched on as soon as the aircraft reaches the flare initiation altitude. The aircraft remains in this mode until the final touchdown.

For this investigation, the scope of the automatic landing problem was restricted in two ways. First, the aircraft simulation equations are restricted to three degrees of freedom by considering the longitudinal axis only. This restriction is reasonable in the light of the accident statistics compiled in References [8, 9], which conclude that accidents due to longitudinal errors are fatal more often than accidents due to lateral errors. Second, the system guidance information was assumed to come from error-free sensors and an error-free ILS beam. This is beneficial to maintain simplicity of the automatic control subroutines, since the objective of this study is the effects of wind shear, and not a study of ILS system errors.

CHAPTER II

AIRCRAFT LANDING MODEL

1. Equations of Motion

The two-dimensional model for aircraft motion presented in this section follows the general form developed by Frost [12]. It accounts for both vertical and horizontal mean wind components having both time and spatial variations.

The aircraft trajectory model employed in this study was derived based on the following assumptions:

- a) The earth is flat and non-rotating.
- b) The acceleration of gravity, g , is constant (9.8 m/sec^2).
- c) Air density is constant (1.23 kg/m^3).
- d) The airframe is a rigid body.
- e) The aircraft is constrained to motion in the vertical plane.
- f) The aircraft has a symmetry plane (the x - z plane).
- g) The mass of the aircraft is constant.
- h) Initial flight conditions are for steady-state flight.

Figure 1 illustrates the forces acting on the aircraft. These include:

- \vec{F}_T thrust of the engines
- \vec{L} lift
- \vec{D} drag
- \vec{W} wind velocity
- $m\vec{g}$ gravitational force.

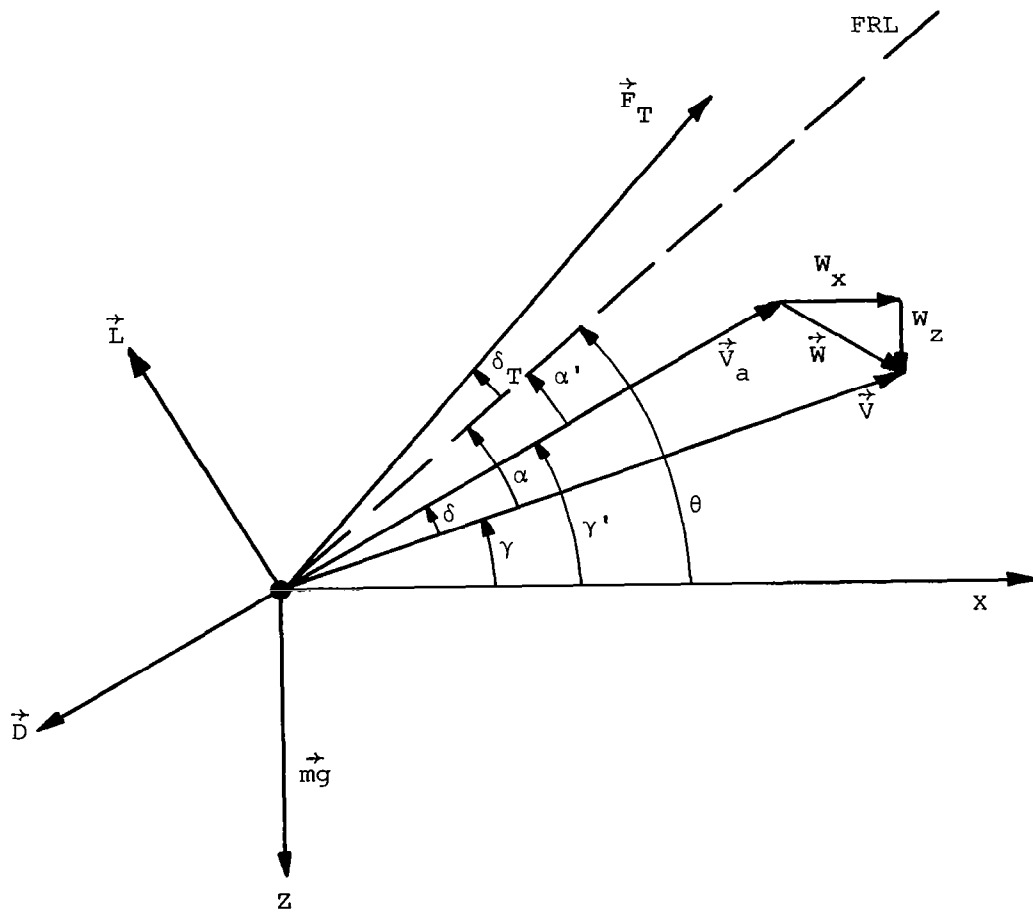


Figure 1 Relationship between the various forces acting on an aircraft [12]

The figure shows the orientation of the forces with respect to the velocity relative to the earth (\vec{V}), the velocity relative to the air mass (\vec{V}_a), and the fuselage reference line (FRL) of the aircraft. The x-axis in Figure 1 is parallel to the surface of the earth and the z-axis is perpendicular to the surface of the earth (positive downward).

From a direct force balance along the direction \vec{V} and along the direction perpendicular to \vec{V} , respectively, it follows from Figure 1 that

$$m\dot{V} = -L \sin \delta - D \cos \delta - mg \sin \gamma + F_T \cos (\delta_T + \alpha) \quad (1)$$

and

$$mV\dot{\gamma} = L \cos \gamma - D \sin \delta - mg \cos \delta + F_T \sin (\delta_T + \alpha) . \quad (2)$$

The aerodynamic forces and the thrust from the engines exert a pitching moment on the aircraft. The equation describing the momentum balance about y is

$$\dot{q} = \frac{d^2\theta}{dt^2} = \frac{F_T L_T}{I_{yy}} + \frac{M}{I_{yy}} , \quad (3)$$

where the dot refers to the derivative with respect to time, and

g is the magnitude of the acceleration of gravity,

V is the magnitude of the velocity relative to the earth,

γ is the angle between \vec{V} and the x-axis (the flight path angle),

F_T is the magnitude of the thrust vector,

m is the aircraft mass,

δ_T is the angle between the thrust vector and the fuselage reference line (FRL),
 α is the angle between \vec{V} and the FRL,
 δ is the angle between \vec{V}_a and \vec{V} ,
 \dot{q} is the time derivative of the pitching rate, q ,
 L_T is the effective moment arm of the thrust vector,
 M is the pitching moment, and
 I_{yy} is the moment of inertia about the symmetry plane of the aircraft.

By considering a different coordinate system in which the x-axis is along the vector \vec{V}_a , called "wind" frame of reference by Etkin [1], similar force equations can be developed by summing up the forces parallel and perpendicular to \vec{V}_a . These are

$$m(\dot{V}_a + \dot{W}_{x_w}) + m q_w W_{z_w} = F_{T_{x_w}} - D - mg \sin \gamma' \quad (4)$$

and

$$m \dot{W}_{z_w} - m q_w (V_a + W_{x_w}) = F_{T_{z_w}} - L + mg \cos \gamma' . \quad (5)$$

It is convenient to express these in terms of the wind components relative to an earth fixed coordinate system, since most wind correlations from the meteorological literature are expressed in such coordinates.

$$W_{x_w} = W_x \cos \gamma' - W_z \sin \gamma' , \quad (6)$$

$$W_{z_w} = W_x \sin \gamma' + W_z \cos \gamma' . \quad (7)$$

Taking the time derivative of W_{X_W} , we get

$$\dot{W}_{X_W} = \dot{W}_X \cos \gamma' - \dot{W}_Z \sin \gamma' - W_X \sin \gamma' \frac{d\gamma'}{dt} - W_Z \cos \gamma' \frac{d\gamma'}{dt} . \quad (8)$$

Then, since $q_W = \frac{d\gamma'}{dt}$,

$$\dot{W}_{X_W} = \dot{W}_X \cos \gamma' - \dot{W}_Z \sin \gamma' - W_{Z_W} q_W . \quad (9)$$

Also, since

$$F_{T_{X_W}} = F_T \cos(\delta_T + \alpha') , \text{ and}$$

$$F_{T_{Z_W}} = F_T \sin(\delta_T + \alpha') ,$$

Equation (4) becomes

$$m\dot{V}_a = F_T \cos(\delta_T + \alpha') - D - mg \sin \gamma' - m(\dot{W}_X \cos \gamma' - \dot{W}_Z \sin \gamma') . \quad (10)$$

From Equation (7), taking the time derivative of W_{Z_W} , we get

$$\dot{W}_{Z_W} = \dot{W}_X \sin \gamma' + \dot{W}_Z \cos \gamma' + W_X \cos \gamma' \frac{d\gamma'}{dt} - W_Z \sin \gamma' \frac{d\gamma'}{dt} , \quad (11)$$

and Equation (5) becomes

$$\begin{aligned} -mV_a q_W &= -F_T \sin(\delta_T + \alpha') - L + mg \cos \gamma' \\ &\quad - m(\dot{W}_X \sin \gamma' + \dot{W}_Z \cos \gamma') . \end{aligned} \quad (12)$$

The moment equation remains the same as Equation (3). The governing force equations in "wind" frame of reference are thus

$$m\dot{V}_a = F_T \cos(\delta_T + \alpha') - D - mg \sin \gamma' - m(\dot{W}_x \cos \gamma' - \dot{W}_z \sin \gamma') , \quad (13)$$

$$mV_a \dot{\gamma}' = F_T \sin(\delta_T + \alpha') + L - mg \cos \gamma' + m(\dot{W}_x \sin \gamma' + \dot{W}_z \cos \gamma') , \quad (14)$$

$$q_w = \frac{F_T L_T}{I_{yy}} + \frac{M}{I_{yy}} , \quad (15)$$

where W_x is the horizontal wind speed, W_z is the vertical wind speed, and α' (the angle of attack) is the angle between \vec{V}_a and the FRL.

2. Incorporation of Wind Shear

The wind is seen to enter the equations in the form of a gradient or wind shear \dot{W}_x and \dot{W}_z . The expanded form of these equations is:

$$\dot{W}_x = \frac{\partial W_x}{\partial t} + \frac{\partial W_x}{\partial X} \frac{dX}{dt} + \frac{\partial W_x}{\partial Z} \frac{dZ}{dt}$$

or

$$\dot{W}_x = \frac{\partial W_x}{\partial t} + V \left[\cos \gamma \frac{\partial W_x}{\partial X} - \sin \gamma \frac{\partial W_x}{\partial Z} \right] , \quad (16)$$

and, similarly,

$$\dot{W}_z = \frac{\partial W_z}{\partial t} + V \left[\cos \gamma \frac{\partial W_z}{\partial X} - \sin \gamma \frac{\partial W_z}{\partial Z} \right] . \quad (17)$$

Thus, both spatial variations and temporal variations in atmospheric motion influence the equations in the wind coordinate system.

Generally, care is needed in evaluating $\frac{\partial W_x}{\partial Z}$ and $\frac{\partial W_z}{\partial Z}$ since the wind speed is normally expressed in terms of altitude measured upward from the surface of the earth, whereas in aerodynamic coordinates, Z is measured downward.

Additional kinematic relationships necessary to solve for the aircraft motion are as follows:

The relative velocity as a function of inertial and wind velocity is

$$V_a = [(\dot{X} - W_x)^2 + (\dot{Z} - W_z)^2]^{1/2}, \quad (18)$$

and, in turn,

$$V = W_x \cos \gamma - W_z \sin \gamma + [(W_z \sin \gamma - W_x \cos \gamma)^2 + V_a^2 - (W_x^2 + W_z^2)]^{1/2}. \quad (19)$$

The angle between \vec{V} and \vec{V}_a is given by

$$\sin \delta = \frac{W_x \sin \gamma + W_z \cos \gamma}{V_a}. \quad (20)$$

Other angular relationships are

$$\alpha' = \theta - \gamma - \delta = \theta - \gamma', \quad (21)$$

$$\alpha = \theta - \gamma. \quad (22)$$

The derivative of α' is

$$\dot{\alpha}' = \dot{\theta} - \dot{\gamma}' = q - \dot{\gamma}',$$

where γ' is given by Equation (14), hence,

$$\begin{aligned} \dot{\alpha}' = q - \frac{F_T \sin(\delta_T + \alpha')}{mV_a} - \frac{L}{mV_a} \\ + \frac{g \cos \gamma'}{V_a} + \frac{1}{V_a} [\dot{W}_x \sin \gamma' + \dot{W}_z \cos \gamma'] . \end{aligned} \quad (23)$$

Also required for solution of the preceding equations are the aerodynamic coefficients

$$\begin{aligned} C_L &= C_L (\alpha', \delta_E, V_a, q, \dot{\alpha}') , \\ C_D &= C_D (\alpha', \delta_E, V_a, q, \dot{\alpha}', C_L) , \\ C_m &= C_m (\alpha', \delta_E, V_a, q, \dot{\alpha}') , \end{aligned} \quad (24)$$

where δ_E is the elevator deflection angle. As indicated above, the aerodynamic coefficients are functions of a number of variables. The expressions for C_L , C_D , and C_m , along with the stability derivative data and aircraft physical data are given in the Appendix.

The equations of motion discussed in this chapter can be solved for the flight of an aircraft flying through spatially and temporally varying two-dimensional wind fields. In this study we have used three different wind shear models,

- 1) atmospheric flow over homogeneous terrain,
- 2) atmospheric flow over buildings, and
- 3) atmospheric flow associated with thunderstorm gust fronts.

The initial conditions used in this simulation are for that of a pitch stabilized aircraft, given by

Altitude = 91 m

$$V_a = 70 \text{ m/sec}$$

$$\dot{V}_a = 0$$

$$\dot{\gamma}' = 0$$

$$\dot{q} = 0$$

$$q = 0$$

$$\dot{\alpha}' = 0.$$

Under these conditions the initial values of thrust, elevator angle and angle of attack were calculated from Equations (13), (14) and (15).

CHAPTER III

MATHEMATICAL MODELS FOR VARIABLE WIND FIELDS

1. Atmospheric Flow Over a Homogeneous Terrain

The mean velocity in the region of the atmosphere near the ground is described by a logarithmic function of altitude. The surface roughness characteristic of most natural terrains is generally described in terms of a vertical scale, Z_0 . For a neutral atmosphere, experimental evidence [18, 19] confirms that the mean wind velocity in the region near the ground can be described by a logarithmic wind profile (Figure 2). The logarithmic wind profile is thus [20], given as a function of altitude Z ,

$$W_x(z) = \frac{u_*}{\kappa} \ln \left(\frac{Z + Z_0}{Z_0} \right), \quad (25)$$

where Z_0 represents the surface roughness, and κ is von Karman's constant. u_* is the friction velocity given by $u_* = \sqrt{\frac{\tau_0}{\rho}}$, where τ_0 is the surface shear stress, and ρ is the air density. Observed wind profiles up to 150 m, over reasonably level and uniformly rough terrain, with neutrally stable conditions, obey this law reasonably well [20].

2. Atmospheric Flow Over Buildings

Since the wind shear models for the flow over a block building and a step are completely described by Sheih, et al. [22] and Bitte

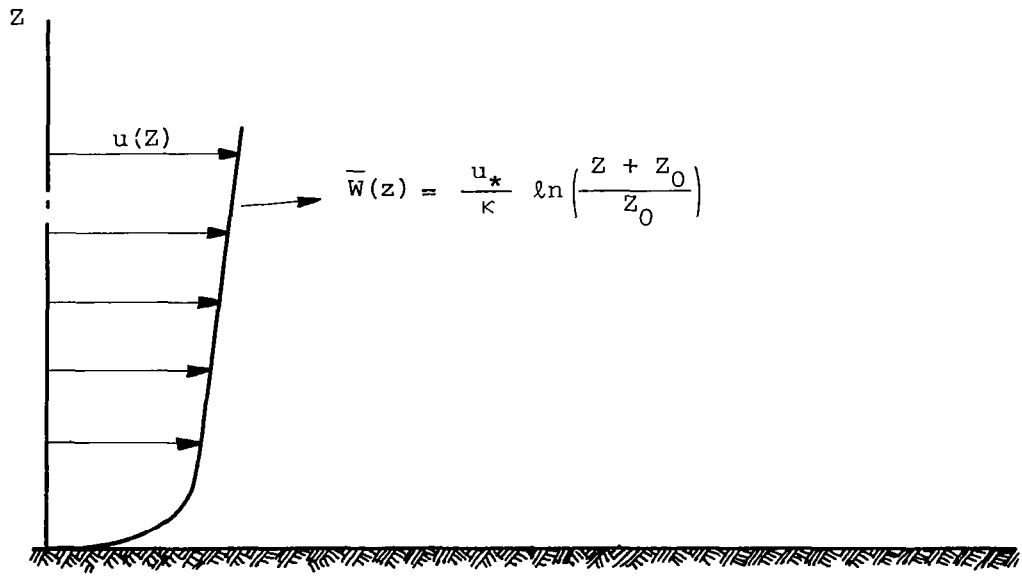


Figure 2 Logarithmic wind profile

and Frost [23], respectively, only a cursory description of the models is presented here.

The distorted shear flows approaching and passing over a building can be divided into a displacement zone, an upstream bubble or downwash zone, and a wake zone which includes the rear separation bubble or cavity zone (see Figure 3). The effect of shear in the approaching flow creates a downwash on the front face and a swirling flow in the wake or cavity zone. Undisturbed, neutrally stable atmospheric wind perpendicular to the axis of the building is assumed far upstream and far downstream of the obstacle (see Figures 4 and 5). The atmospheric wind field is analyzed by using the Navier-Stokes equations with a two-equation model, one for the turbulence kinetic energy and the other for turbulence length scale. In this approach, the partial differential equations for the vorticity, stream function, turbulence kinetic energy, and turbulence length scale are solved by a finite-difference technique.

Both vorticity contours (Figure 6) and streamline patterns (Figure 7) confirm the experimental evidence of a small downwash zone near the front lower corner and a large recirculation zone behind the obstruction. Figures 8 and 9 show the computed velocity profiles at selected X -stations in the region close to the wall. The flow is decelerated as it approaches the obstruction and is accelerated as it passes over the obstruction. In the region above the recirculation zone, the flow is accelerated because of the displacement of the flow. The flow re-attaches near $X = 12.3H$ and the logarithmic boundary

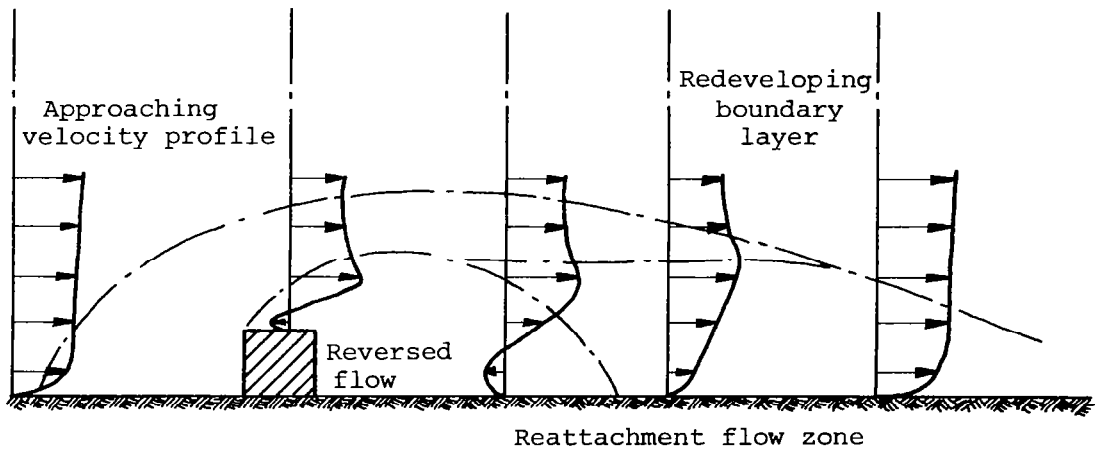
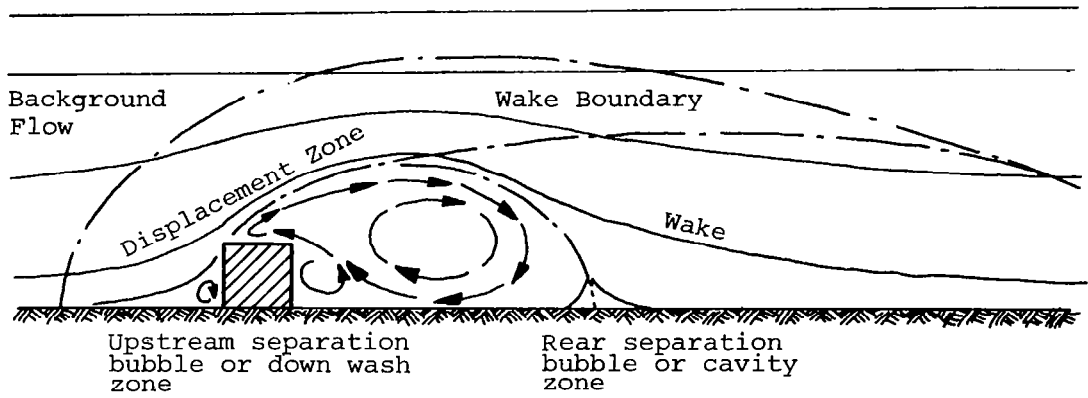


Figure 3 Definition of flow zones near a sharp-edged block [22]

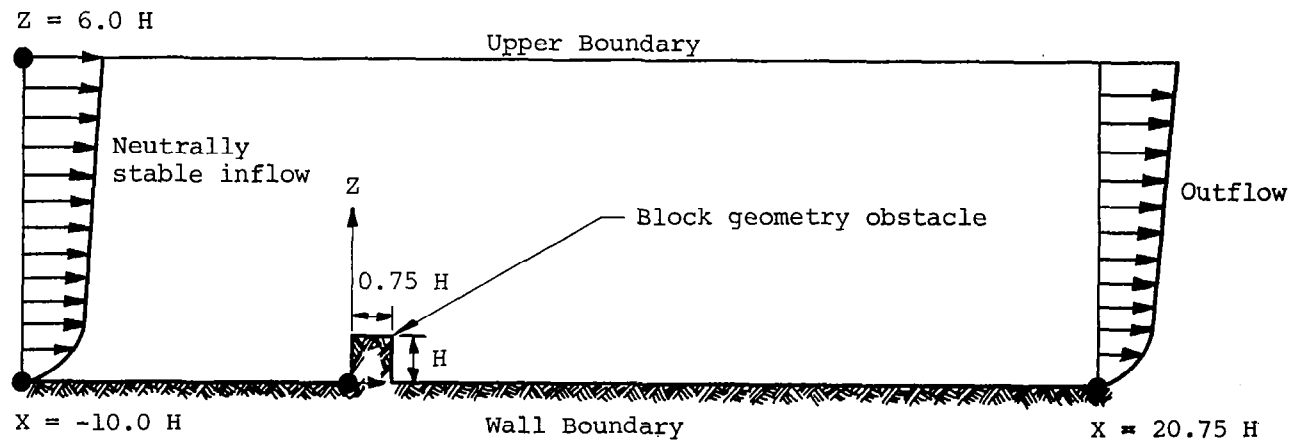


Figure 4 Description of flow region considered for a block building [22]

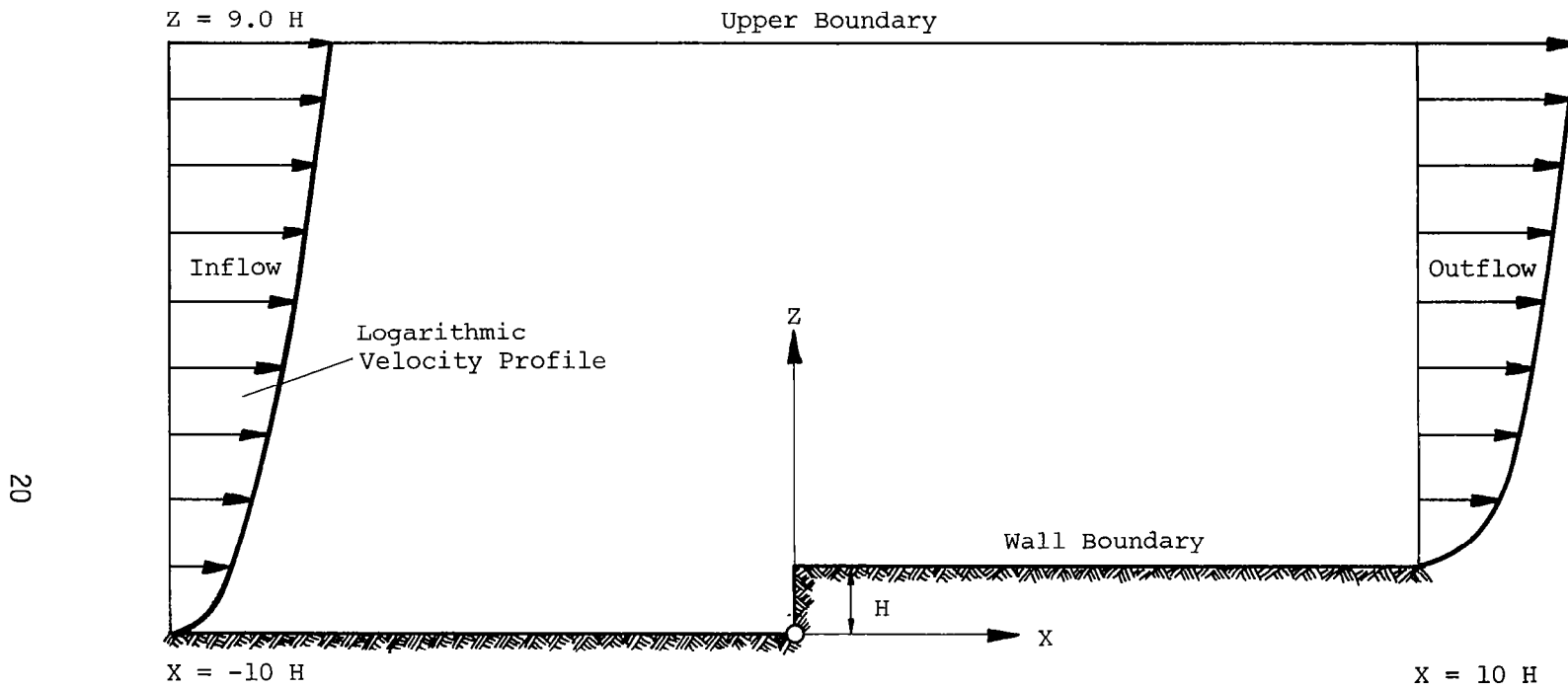


Figure 5 Description of flow region considered for a long, wide building [23]

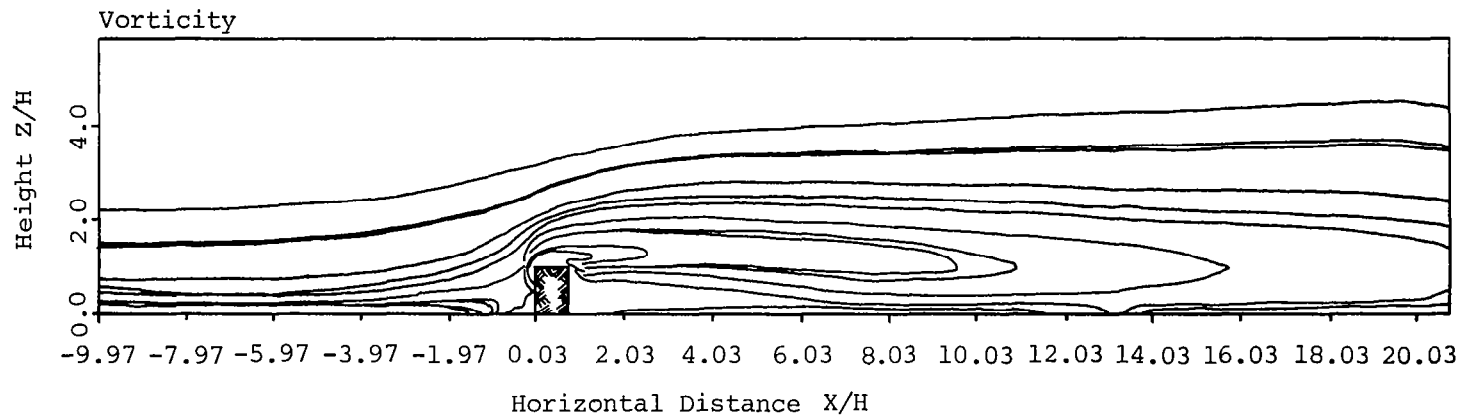


Figure 6 Vorticity contour [22]

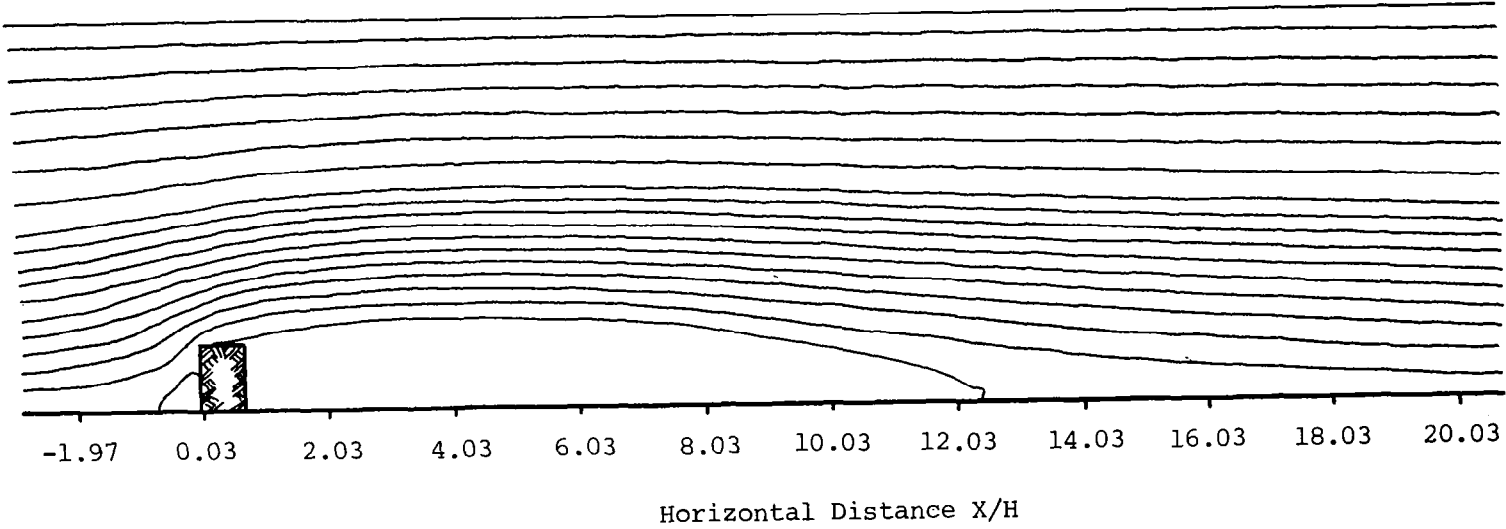


Figure 7 Streamline patterns [22]

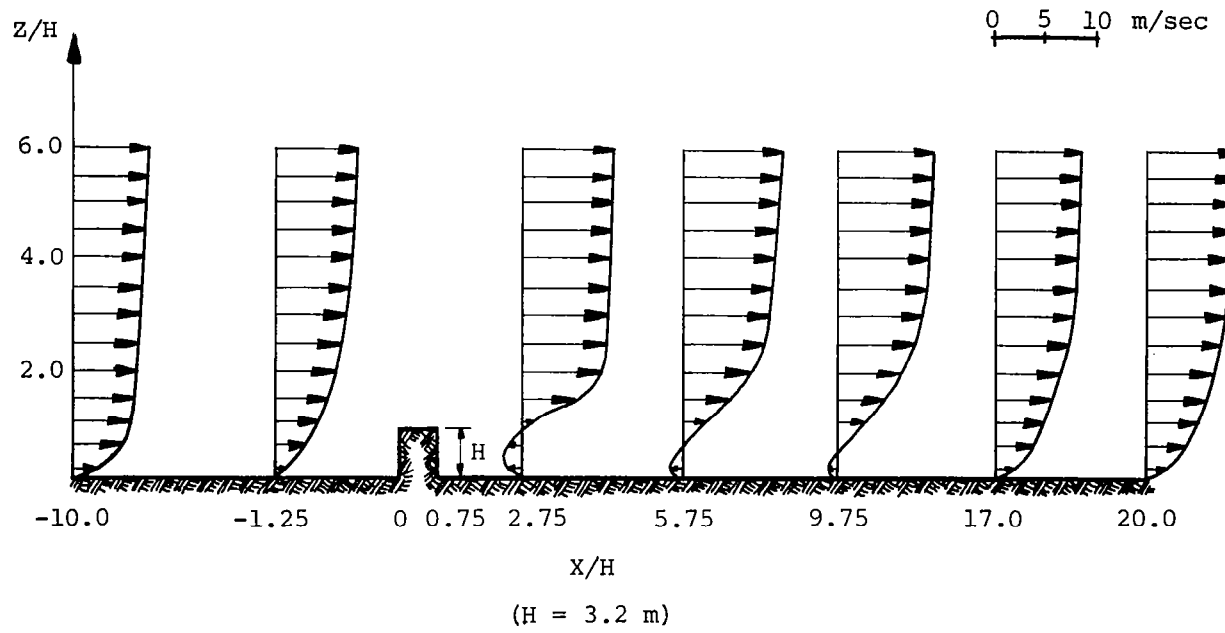


Figure 8 Velocity profiles over an obstruction on the surface [22]

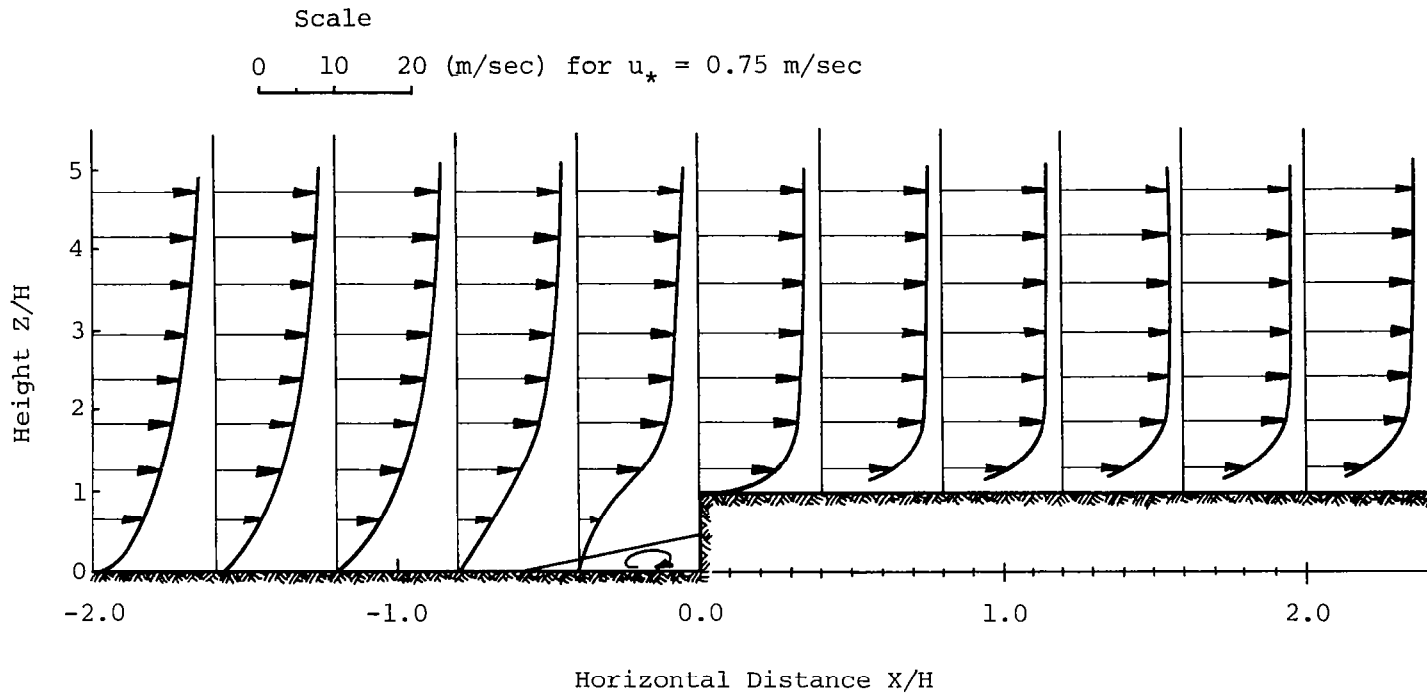


Figure 9 Velocity profiles over a step geometry long wide building [23]

layer begins to re-establish downstream. These results seem to agree very well with the limited experimental data available.

The velocity distributions of the atmospheric flow around buildings are especially important in the design and operational procedures for helicopters and V/STOL aircraft operating in large metropolitan areas.

3. Atmospheric Flow Associated with Thunderstorm Gust Fronts

Gusty winds are undoubtedly the most hazardous for an aircraft to negotiate. One of the most common causes of significant wind shear is the gust front associated with thunderstorms. The thunderstorm gust front is believed responsible for several accidents [5, 22]. The severe wind shear accompanying thunderstorms is generated by a vigorous rain-cooled downdraft, which spreads out horizontally from the storm cell as it approaches the ground. The cold outflow is led by a strong, gusty wind which often occurs as much as 16 km ahead of the storm, called the gust front.

Mathematical schemes for computing wind fields associated with thunderstorm gust fronts are still in the formative stages. After extensive study of gust front characteristics and the available gust front data, Fichtl and Camp [26] have presented a mathematical model which describes updrafts and downdrafts associated with gust fronts along a given approach path. This model incorporates both scaled vertical wind speeds along a -2.7 degree glide slope from the gust front data of Goff [27], and the vertical wind speeds reconstructed from the digital flight data record of Eastern 66 [8]. The sequence

of vertical wind speeds encountered by an aircraft during landing is given by the following:

Major downdraft:

$$W_z = - P_1 A \sin \left(\pi \frac{X - X_r}{q_1} \right) ; Z_D \geq Z > Z_r$$

Major updraft:

$$W_z = A \frac{(1 - 2q_0)(X - X_r)^3 + (1 - 3q_0^2)(X - X_r)^2 + (2q_0 - 3q_0^2)(X - X_r)}{-q_0^2(q_0 - 1)^2} ; Z_r \geq Z \geq Z_r - L'$$

Minor downdraft:

$$W_z = - P_2 A \sin \left(\pi \frac{X_r - 1 - X}{q_2} \right) ; (Z_r - L) > Z \geq (Z_r - (1 + q_2) L')$$

Minor updraft:

$$W_z = P_2 A \sin \left(\pi \frac{X_r - 1 - X}{q_2} \right) ; [Z_r - (1 + q_2) L'] > Z \geq [Z_r - (1 + 2q_2) L']$$

where

$$X_r = \frac{Z_r}{L'} ; X = \frac{Z}{L'}$$

The various quantities in the above equations are defined as follows:

W_z = thunderstorm cold air downdraft,

Z = vertical coordinate,

Z_D = altitude of the top of the major downdraft,

- Z_r = altitude of the top of the major updraft,
 Z_B = altitude of the bottom of the minor downdraft,
 A = amplitude of major vertical velocity updraft,
 L' = vertical extent of major vertical velocity updraft relative
to the flight path,
 P_1 = ratio of major downdraft to major updraft velocities,
 P_2 = ratio of minor downdraft or minor updraft to major updraft
velocity,
 $q_0 = (Z_r - Z_m)/L'$,
 $q_1 = (Z_r - Z_D)/L'$,
 $q_2 = (Z_r - Z_B - L')/L'$.

The values for the cold air outflow parameters used in this simulation study are that of typical vertical wind speeds derived for data provided by NOAA/NSSL [27]:

- $L' = 91 \text{ m}$
 $Z_R = 152 \text{ m}$
 $A = 15.0$
 $P_1 = 1.2$
 $P_2 = 0.35$
 $q_0 = -0.36$
 $q_1 = 2.0$
 $q_2 = 2.3.$

In this wind shear model, the vertical winds due to the thunderstorm gust front described above are superimposed on a stable

atmospheric boundary layer. The mean wind velocity under stable conditions is given by

$$W_x(z) = \frac{u_*}{\kappa} \left(\ln \left(\frac{z + z_0}{z_0} \right) + 5.2 \frac{z}{\hat{L}} \right),$$

where \hat{L} is the Monin-Obukhov stability length.

CHAPTER IV

AUTOMATIC CONTROL SYSTEM

The two principal quantities that need to be controlled in symmetric flight are speed and flight path angle, i.e., the vehicle velocity. To achieve this, control forces are needed both parallel and perpendicular to the flight path. Parallel force is provided by thrust or drag control, and perpendicular force by lift control achieved via elevator deflection. It is evident from simple physical reasoning (or from the equations of motion) that the main initial response to opening the throttle (increasing the thrust) is a forward acceleration, i.e., speed control. The main initial response to elevator deflection is a rotation in pitch, with subsequent changes in angle of attack and lift, and hence, development of $\dot{\gamma}$, a rate of change of flight path angle. When the transients that follow such control actions have died away, a new steady state is achieved.

In this section the longitudinal automatic landing system will be described, and some of the design considerations will be given.

It has been shown in Reference [24] that turbulence causes larger deviations from the desired flight path than the errors in ILS guidance. This study, therefore, concentrates on the effect of wind shear on safe automatic landings. The system guidance information is assumed to come from an error-free ILS beam and altimeter. Reference [3] has an excellent discussion on longitudinal automatic landing and aircraft control laws. The overall control system can be represented

in the form of a block diagram as shown in Figure 10. The flight control laws are segmented into control modes for different portions of the approach and landing,

In the various control modes the linear filters are described by transfer functions. The filtering function, however, is actually performed in the digital computer by solving difference equations.

Simulating a linear system with the appropriate difference equation is more efficient than solving the differential equations directly by numerical integration. Numerical integration would be rather a lengthy process and may be unstable for large sampling intervals [3]. The difference equation for one of the linear filters used in this simulation can be derived as follows:

$$G(s) = \frac{Y(s)}{X(s)} = \frac{Ks}{s+a} .$$

The response of the filter to a unit step input is

$$Y(s) = \frac{Ks}{s+a} \frac{1}{s} = \frac{K}{s+a} \quad \text{or} \quad y(t) = K e^{-at} \delta(t) .$$

Taking the z-transform,

$$y(z) = \frac{Kz}{z - e^{-aT}} .$$

Factoring the z-transform of a unit step function from $y(z)$,

$$y(z) = K \frac{z-1}{z - e^{-aT}} \frac{z}{z-1} .$$

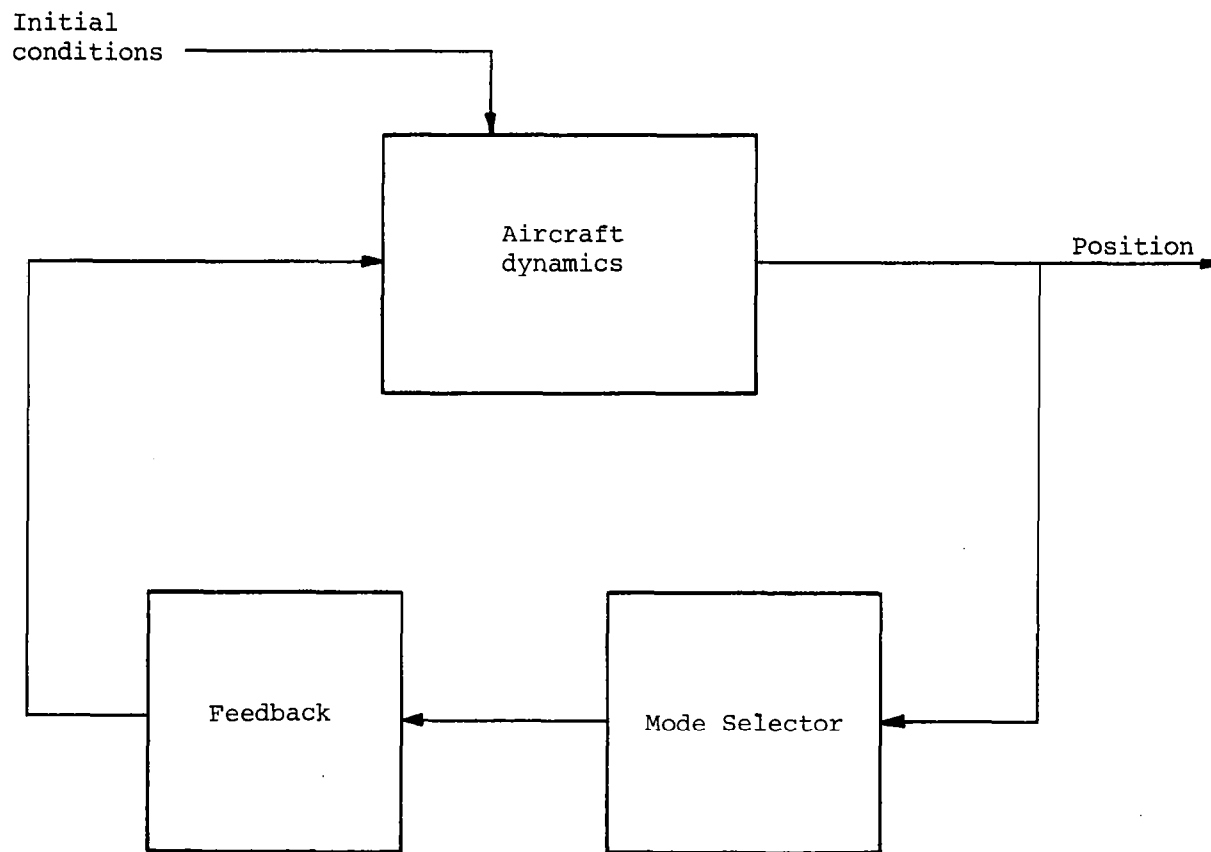


Figure 10 Overall block diagram of control system

Since the response to a general input is wanted, replace the step input by a general input $x(z)$. The actual input is approximated by a linear combination of unit step functions and is equal to the general input at the sampling points,

$$y(z) = K \frac{z-1}{z-e^{-aT}} x(z) .$$

Cross-multiplying,

$$(z - e^{-aT}) y(z) = K(z - 1) x(z) .$$

Dividing throughout by z ,

$$\left(1 - \frac{e^{-aT}}{z}\right) y(z) = K \left(1 - \frac{1}{z}\right) x(z) .$$

Transforming to the discrete time domain,

$$y_n - e^{-aT} y_{n-1} = K(x_n - x_{n-1}) ,$$

and rearranging, the final form of the difference equation is obtained,

$$y_n = e^{-aT} y_{n-1} + K(x_n - x_{n-1}) .$$

At the sampling points the difference equation is the exact solution for the response of the equivalent analog system. The difference equations for the various filters were compared to those obtained using numerical integration (fourth-order Adams-Bashford); it was concluded that the computation efficiency of the difference

equations is better than that of the numerical integration technique [3].

1. Mode Selector

The mode selector automatically selects the proper control mode in sequence (i.e., the altitude hold, glide slope capture, glide-slope tracking, and flare mode) according to predetermined criteria defined by the desired flight path.

In accordance with conventional practice [25], the control modes operate on the velocity and pitch stabilized aircraft and therefore operate with only two command variables: speed command, V_c , and pitch angle command, θ_c .

The mode selector is best described by considering a landing approach (see Figure 11) and the flow chart (Figure 12). The aircraft approaches the ILS glide slope at a constant altitude of 91 m until the aircraft intercepts the ILS beam. During this time the mode selector maintains Mode 1, i.e., the altitude hold mode. As soon as the aircraft penetrates the ILS beam, the mode selector compares the aircraft position to the point of intersection of the horizontal flight path and the ILS glide slope; when the aircraft reaches that point it switches to Mode 2, the capture mode. The capture mode is timed and the flight path angle is compared with the desired glide slope; as soon as the desired glide slope is reached the mode selector switches to Mode 3, the glide-slope tracking mode. Glide-slope tracking proceeds to a preselected altitude, at which point the sink rate and velocity of the aircraft are used to calculate the flare

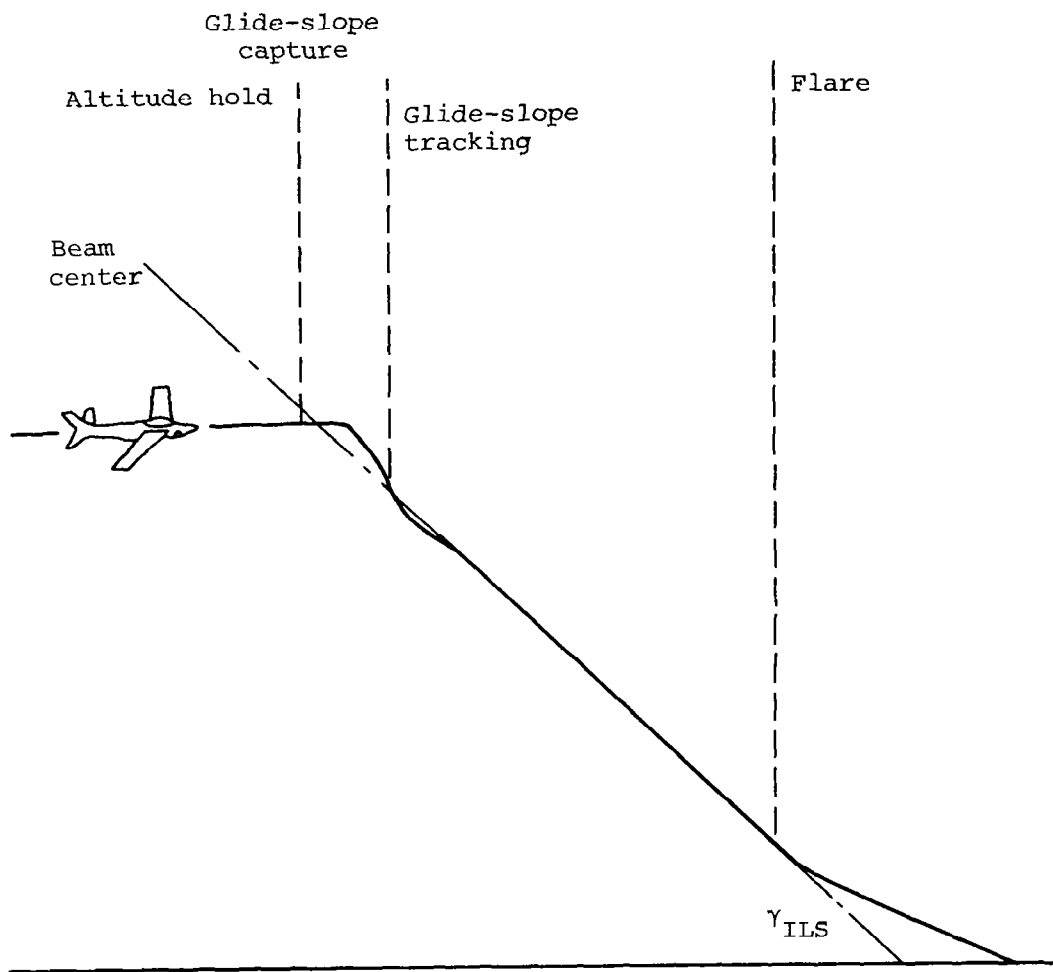


Figure 11 Automatic landing geometry using ILS

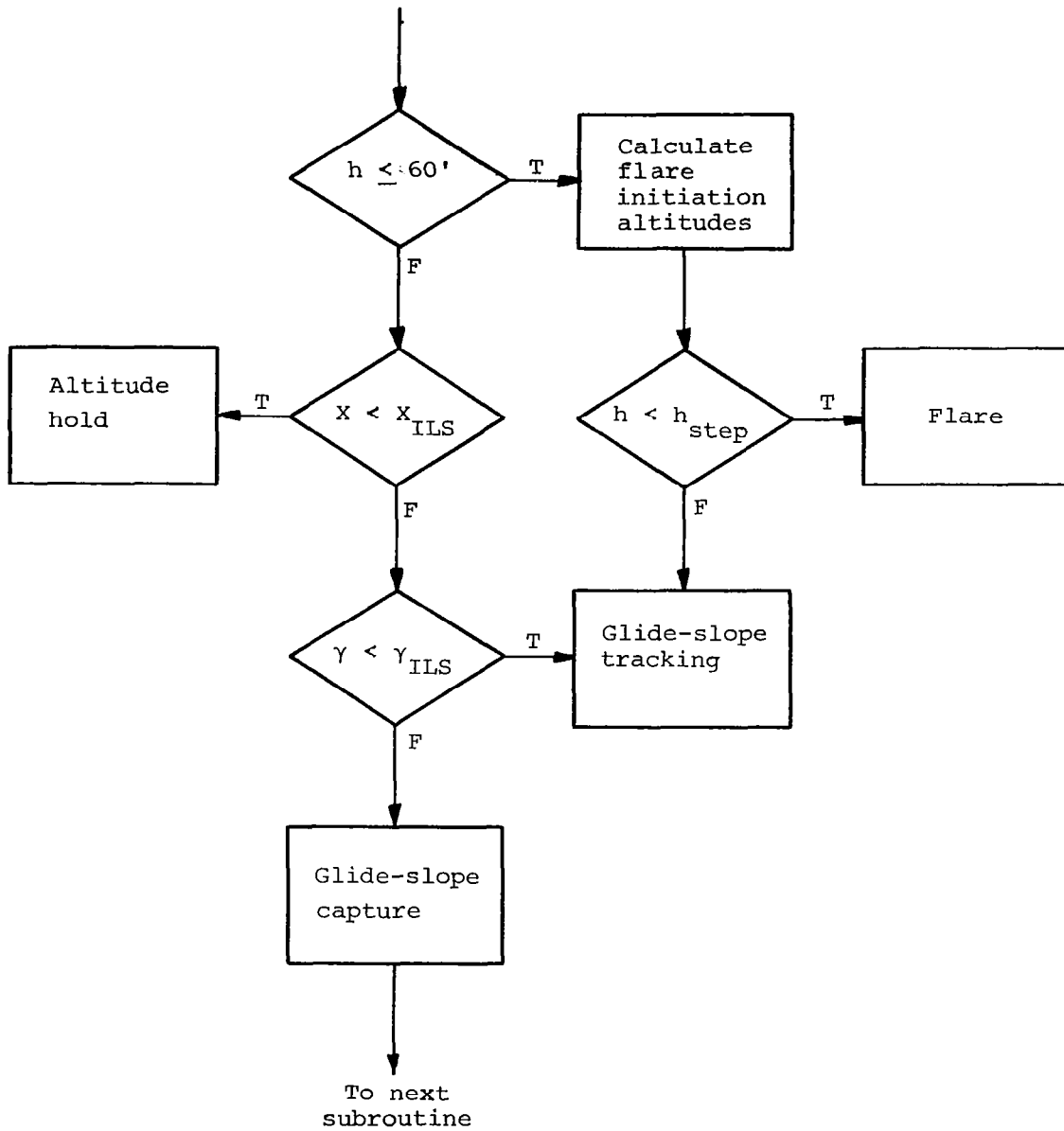


Figure 12 Mode control logic

initiation altitude (h_{step}) and other initiation parameters described in the flare-mode selection. The mode selector then switches to Mode 4, the flare mode, when h_{step} is reached.

Notice that no automatic go-around mode is provided; the simulated aircraft is forced to land so that the conditions can be found that result in unsatisfactory landings.

2. Altitude Hold Mode

A simple hold mode incorporated in the system keeps the aircraft flying at a constant altitude. The digital control was modeled after the representative analog system shown in Figure 13. The system consists of a differencing circuit for calculating the altitude error, Δh , followed by a low pass filter, a gain, and a low gain integrator. For comparison, digital equivalent equations are as follows:

$$\theta_{c_j} = c_1 \theta_{c_{j-1}} + c_2 \theta_{c_{j-2}} + c_3 \Delta h_j + c_y \Delta h_{j-1} ,$$

$$\Delta h_j = h_j - h_{\text{ref}} ,$$

$$\theta_j = c_1 \theta_{j-1} + c_2 \Delta h_{j-1} ,$$

$$\theta_{c_j} = \theta_{c_{j-1}} + k_2 \theta_j + c_3 \theta_{j-1} .$$

These equations are solved once each computation cycle. The constants, c_1 , c_2 and c_3 , are given by

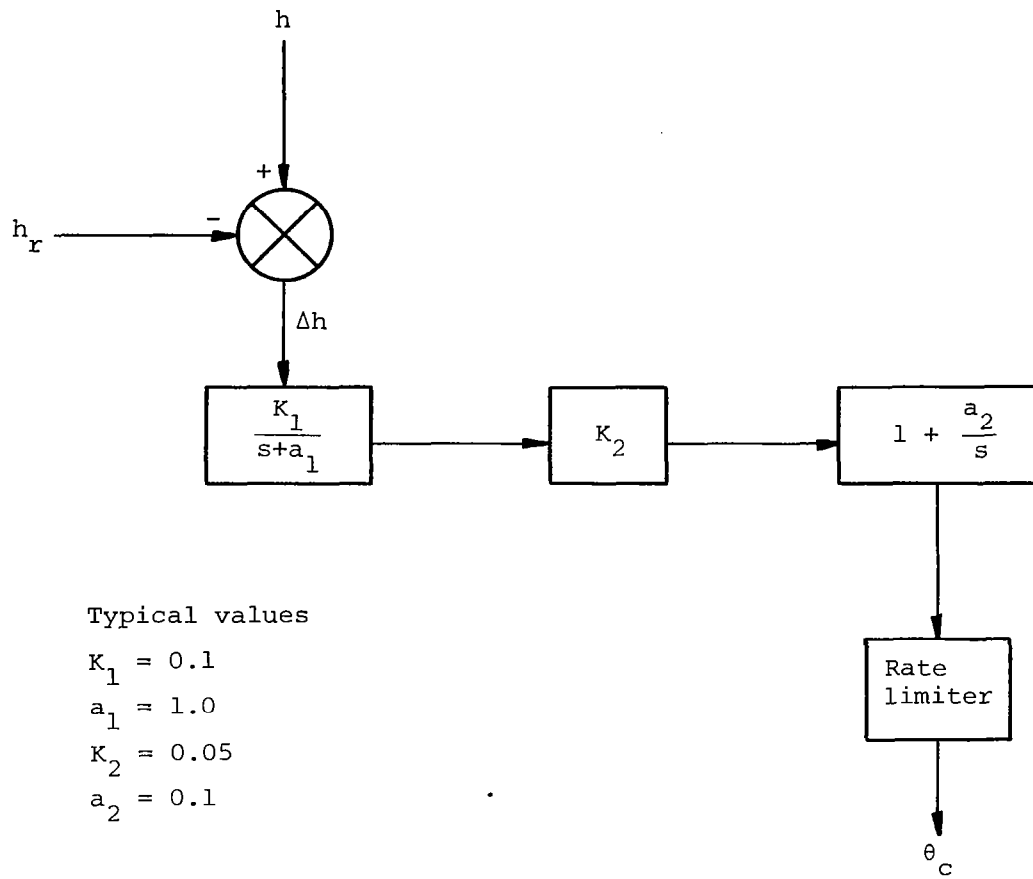


Figure 13 Altitude hold mode

$$c_1 = e^{-a_1 T} ,$$

$$c_2 = \frac{k_1}{a_1} (1 - c_1) ,$$

$$c_3 = k_2 (a_2 T - 1) ,$$

where T is the sampling interval.

3. Capture Mode

The capture mode (Figure 14) provides for a smooth rotation from level flight to the glide-slope angle. In this mode a step pitch angle command, $\Delta\theta_p$, is applied to rotate the airplane. The magnitude of the step is based upon the glide slope angle of the beam to be captured. In addition, an inertial vertical velocity error signal is generated to increase the sink rate for a given glide-slope angle. The error signal, θ_ϵ , is then integrated and filtered to produce the pitch angle command. The integrator provides an error signal proportional to the altitude error. Since the sink rate reference value is the proper sink rate of the aircraft on the glide slope, the resulting altitude reference is a parabolic curve that smoothly intersects the glide slope.

The difference equations are as follows:

$$\theta_{\epsilon_j} = h_c - h_j ,$$

$$\theta_{c_j} = c_1 \theta_{c_{j-1}} - c_2 \theta_{c_{j-2}} + c_3 \theta_{\epsilon_{j-1}} + c_4 \theta_{\epsilon_{j-2}} + \Delta\theta_p ,$$

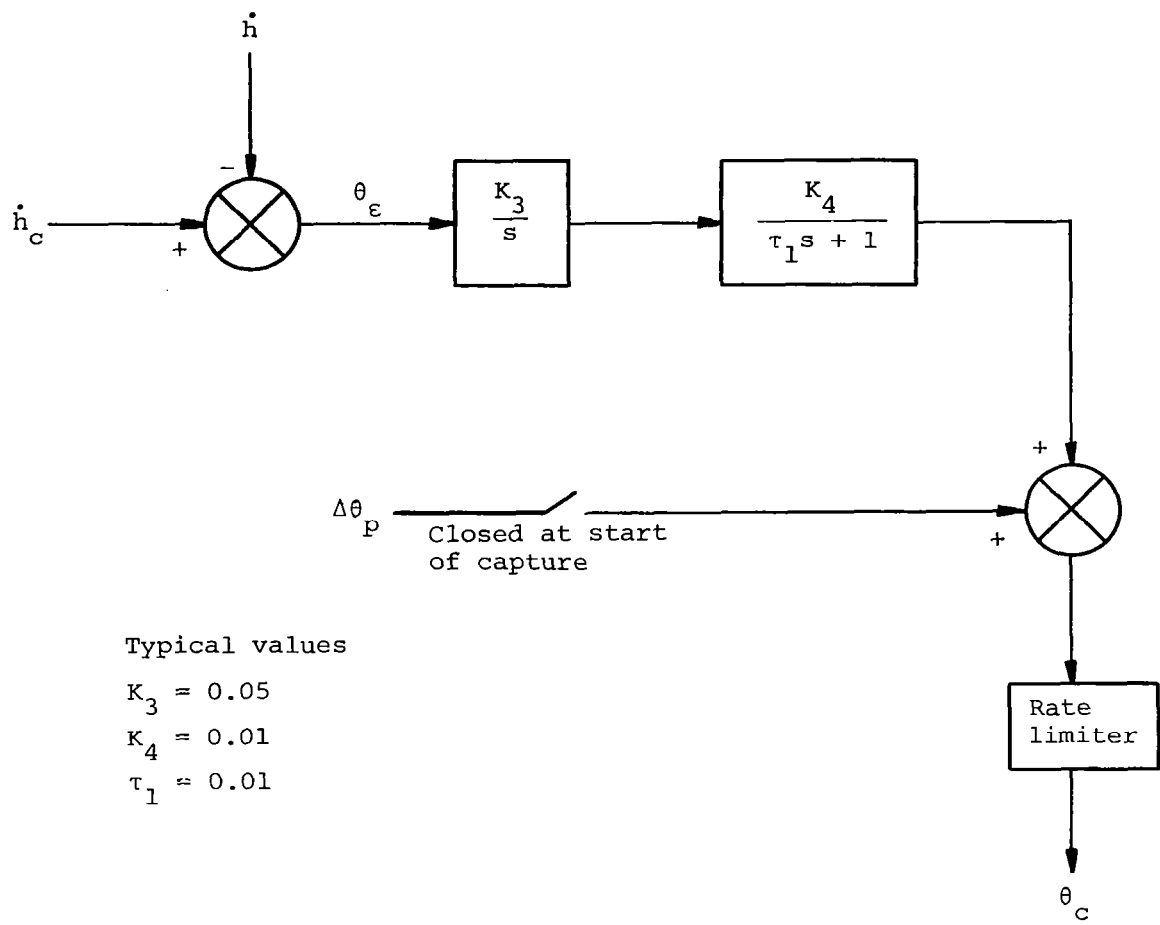


Figure 14 Glide slope capture mode

where

$$c_1 = 1 + c^{-T/\tau} ,$$

$$c_2 = e^{-T/\tau} ,$$

$$c_3 = k_3 k_4 [T + \tau_1 (c_2 - 1)] ,$$

$$c_4 = k_3 k_4 [\tau - c_2 (T + \tau)] .$$

4. Glide-Slope Tracking Mode

After glide-slope capture the aircraft remains in the glide-slope tracking mode (Figure 15) until flare. The glide-slope error angle, ϵ , is passed through a low-pass filter, a gain, and then a low-gain integrator. In addition, two differencing circuits are used which estimate the approximate altitude error for the next step and give pitch error signal, θ . This extension is a pitch altitude command, θ_c , proportional to $h - h_r$ and also $\dot{h} - \dot{h}_c$, where h_r is the reference altitude and \dot{h}_c is the proper sink rate for the given glide slope. The digital equivalent equations are as follows:

$$\epsilon_j = \gamma_j - \gamma_{ref} ,$$

$$\theta_j = k_4 (h_j - h_r) + k_5 (\dot{h}_j - \dot{h}_c) ,$$

$$\theta_{p_j} = c_1 \theta_{p_{j-1}} + c_2 \epsilon_{j-1} ,$$

$$\theta_{\epsilon_j} = \theta_{\epsilon_{j-1}} + k_6 \theta_{p_j} + c_3 \theta_{p_{j-1}} ,$$

$$\theta_{c_j} = \theta_j + \theta_{\epsilon_j} ,$$

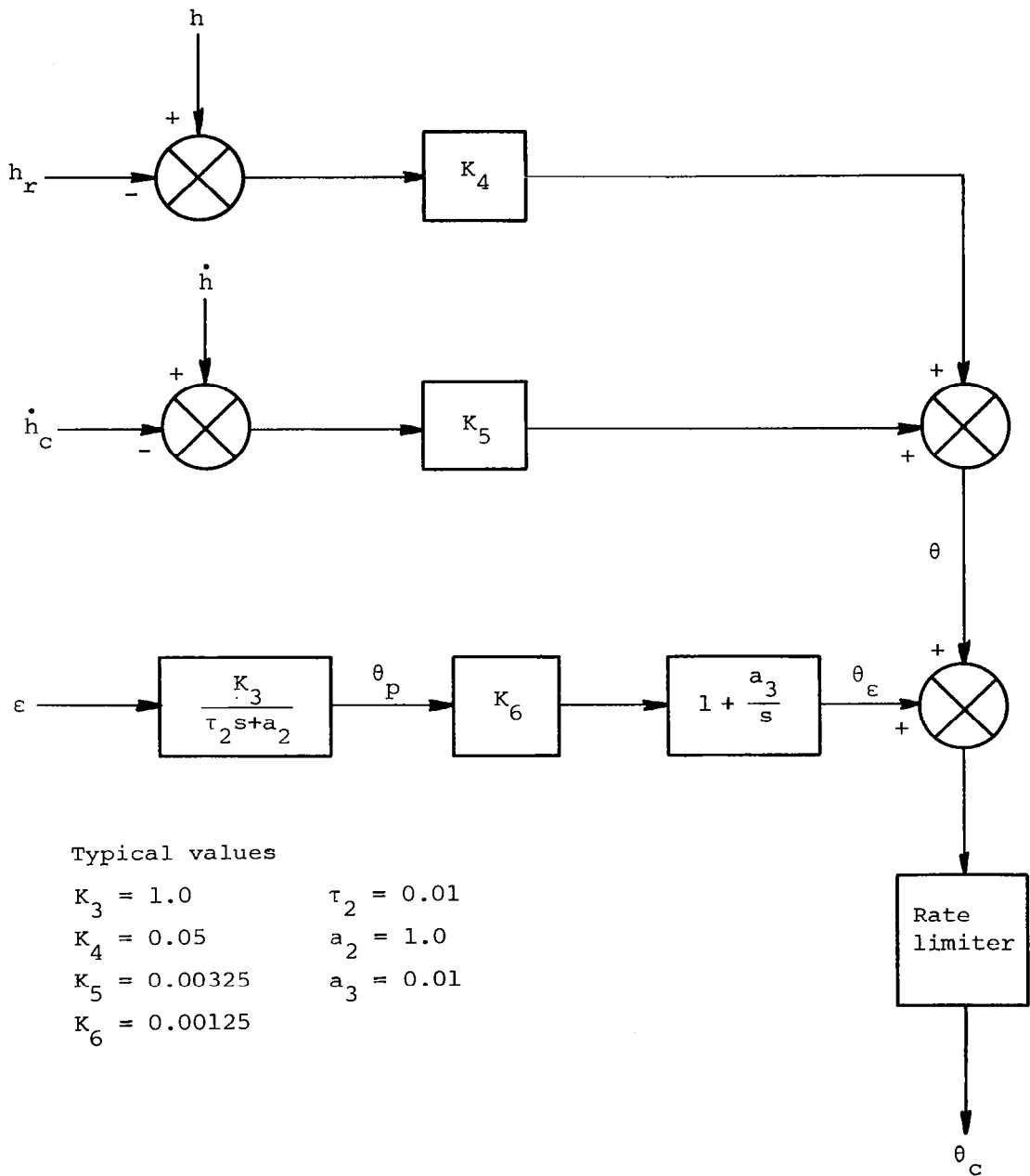


Figure 15 Glide slope tracking mode

where

$$c_1 = e^{-\frac{a_2 T}{\tau_2}},$$

$$c_2 = \frac{k_3}{a_2} (1 - c_1),$$

$$c_3 = k_6 (a_3 T - 1).$$

5. Flare Mode

The flare mode controls the traditional exponential flare [25].

The flare has three boundary conditions,

h_f initiation altitude of feedback control law,

\dot{h}_f initial sink rate,

\dot{h}_{f_0} desired vertical touchdown velocity.

A flare law that satisfies these boundary conditions is developed by Neuman and Foster [3]. A modified version of this flare law is used in our simulation. The equation that satisfies the boundary condition is:

$$h_r(t) = [h_f - a_4 \dot{h}_{f_0}] e^{-t/a_4} + a_4 \dot{h}_{f_0}, \quad (26)$$

and a_4 is calculated as

$$a_4 = h_f / (\dot{h}_f - \dot{h}_{f_0}). \quad (27)$$

The reference sink rate is the derivative of Equation (26),

$$\dot{h}_r = - (1/a_4) (h_f - a_4 \dot{h}_{f_0}) e^{-t/a_4} . \quad (28)$$

The predictive portion of the flare law (Figure 16) has two sections, a step command in pitch, $\Delta\theta_p$, which causes the aircraft to begin to rotate, and a ramp pitch command, $\Delta\theta_R$, which begins somewhat later. With no other disturbance, the predictive flare commands will generate an approximately exponential flare. Feed-back is used to overcome disturbance. Equation (26) is the solution of the following differential equation:

$$h_r \dot{h}_r + a_4 (\dot{h}_r - \dot{h}_{f_0}) = 0 , \quad (29)$$

with the boundary conditions $h_r = h_f$ at $t = 0$, and $\dot{h}_r = \dot{h}_{f_0}$ at $h = 0$. The feed-back version of the flare law generates a corrective signal when Equation (29) is not fulfilled by the actual altitude, h , and sink rate, \dot{h} , in place of h_r and \dot{h}_r . The corrective signal is (see Figure 16):

$$\theta_{fb} = K_f \left[1 + \frac{a_5}{s} \right] [h + a_4 (\dot{h} - \dot{h}_f)] , \quad (30)$$

which is added to the predictive pitch command. Hence, no correction signal is applied when the reference path is followed.

When the flare subroutine is entered for the first time, the sink rate is used to calculate decision altitudes for the predictive flare law commands. The altitudes at which these initial calculations are made are somewhat above the highest value at which the flare may be

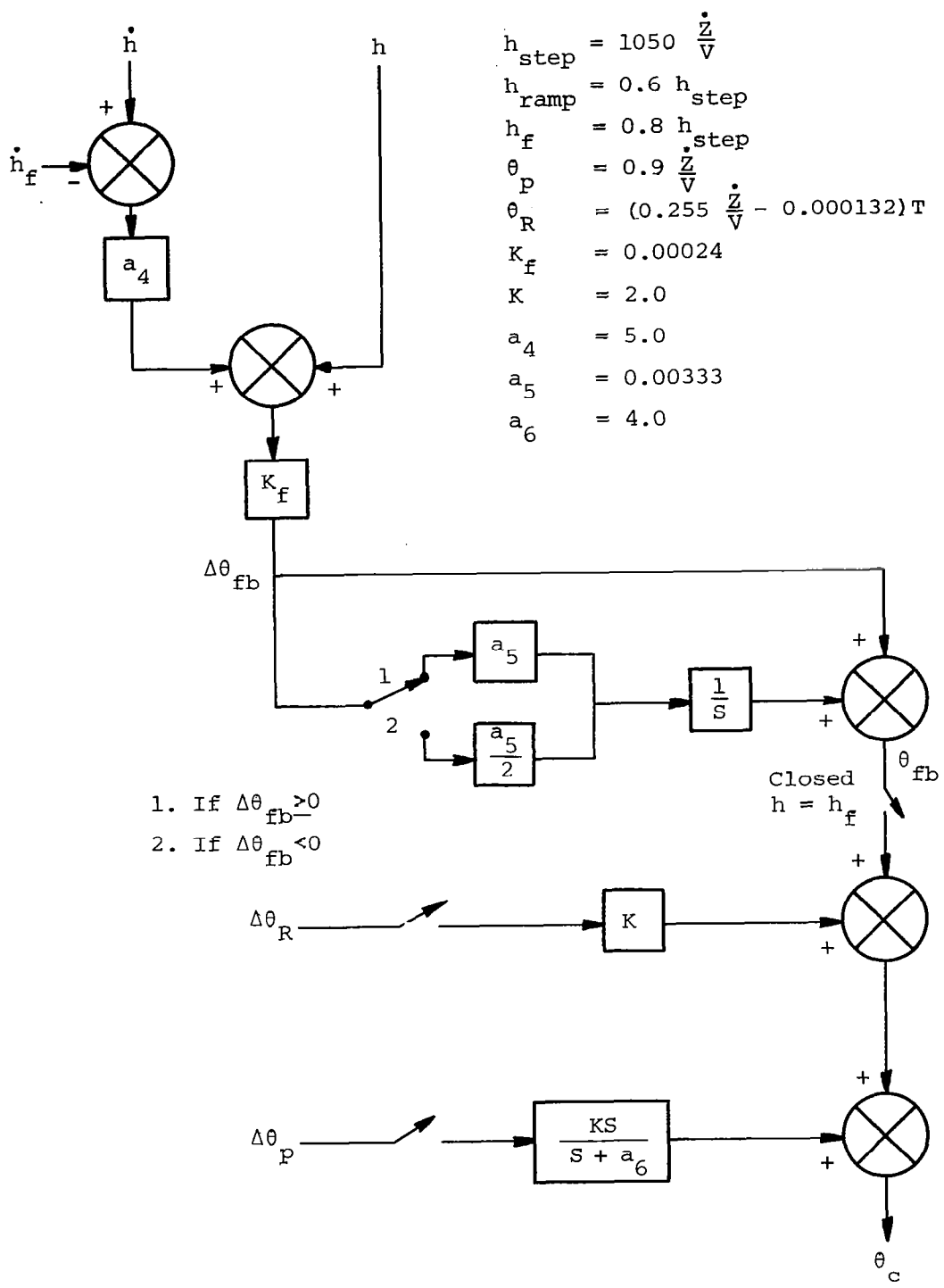


Figure 16 Flare mode

started. The step command altitude is proportional to the flight-path angle, $\gamma \approx \dot{h}/v$. The ramp begins at a proportionally lower altitude. Since the aircraft does not begin to deviate from a straight-line glide path instantaneously, upon receiving the pitch step command, the altitude for the corrective feed-back to begin is also selected proportionally lower than the step command altitude. After these calculations are completed, the flare mode transfers the authority back to the glide-slope tracking control.

When the step command altitude, h_{step} , is reached, the flare control mode takes over completely and from the sink rate, \dot{h} , calculates and executes $\Delta\theta_p$. Then the ramp increment, $\Delta\theta_R$, and the feedback gain constant, a_4 , are calculated. At this point the mode controller is switched to its final submode.

In the final submode the predictive ramp pitch command is added to the corrective feed-back flare command. The summed signals are transmitted as the pitch change command, θ_c .

Under disturbances, the feed-back term in the flare law does not attempt to guide along a path fixed in space, or even hold $h(t)$ and $\theta(t)$ at given values. As long as the feed-back signal of Equation (30) is zero no correction is made. Disturbances, therefore, tend to cause translations of the touchdown point rather than large maneuvers to meet a given touchdown point, which would often cause hard landings.

6. Calculation of the Feed-Back Controls

To control the flight path of an airplane automatically, it would be desirable to control the flight-path angle, γ , directly. However, there is no output control variable that controls γ . In linearized models [1], the steady velocity, \vec{V} , at which the airplane flies is governed by the lift coefficient, which is in turn fixed by the elevator angle, implying that a constant δ_E gives a fixed \vec{V} . Also, the flight path angle, γ , at any given speed is controlled by the thrust in the long term, implying that the ultimate result of moving the throttle at fixed elevator angle is a change in γ without change in speed. But, by physical reasoning [1], we know that initial response to opening the throttle is a forward acceleration, and initial response to elevator deflection is a rotation in pitch; hence, the short term and long term effects of these controls are quite contrary. The total picture of longitudinal control is clearly far from simple when we represent the aircraft motion with a non-linear system of equations.

To make short and long term responses agree, the aircraft is stabilized in the following manner. The speed of the aircraft is kept nearly constant throughout the landing operation and flight path is controlled by means of both throttle and elevator angle deflection. The thrust control loop maintains constant airspeed by generating a thrust command signal to drive the throttle servo (Figure 17). The thrust command signal is derived from airspeed error, horizontal and vertical acceleration, and the pitch command signal. These four signals are processed by passing through variable gains and a

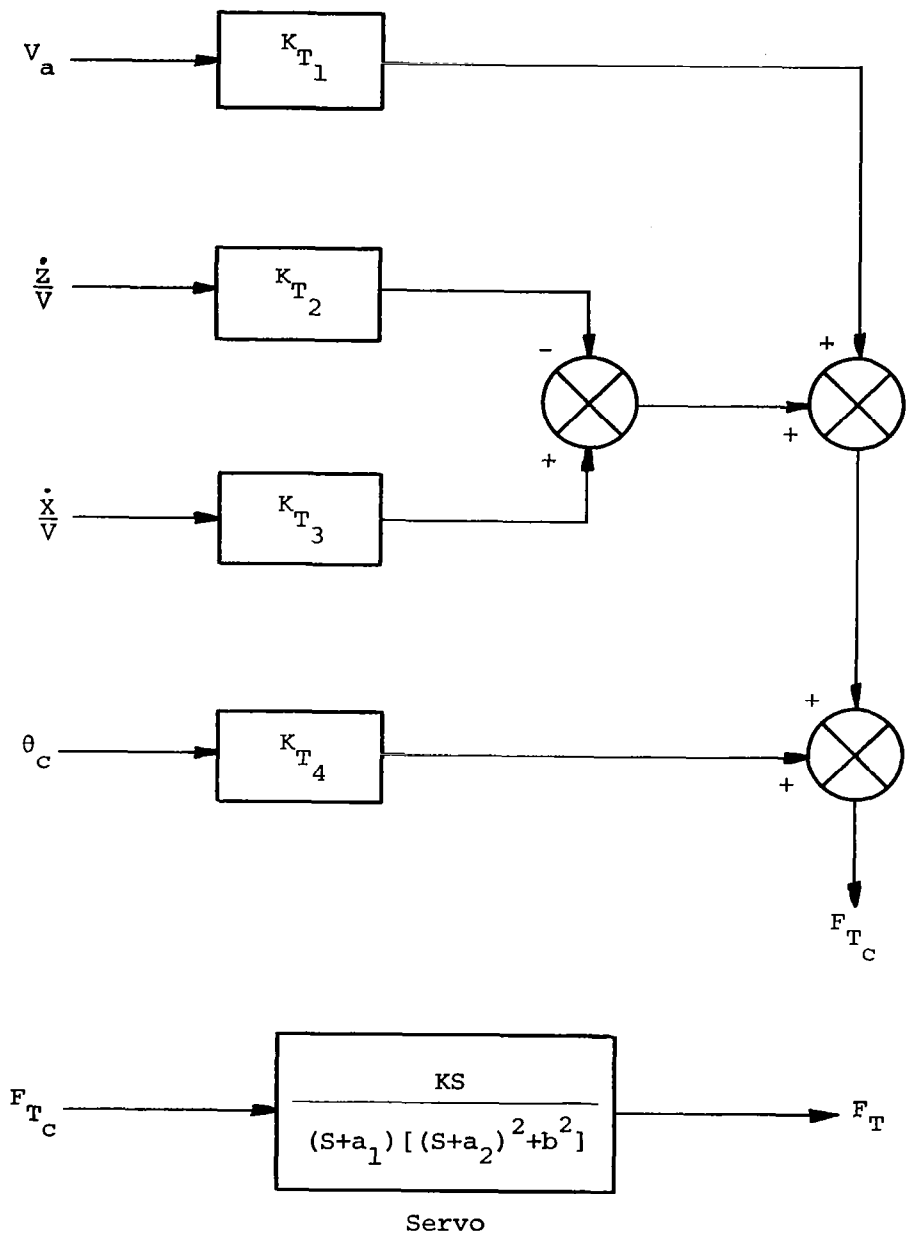


Figure 17 Feedback loop-thrust

differencing circuit so as to generate a thrust command signal of correct magnitude. The elevator control loop generates an elevator angle command signal to drive the elevator angle servo (Figure 18) so as to maintain air velocity constant and control the flight path. The elevator angle command signal is also derived from airspeed error, horizontal and vertical acceleration, and the pitch command signal, and then passed through variable gains. The thrust command signal and elevator angle command signal are given by

$$F_{T_C} = K_{T1} V_a - K_{T2} \frac{\dot{z}}{V} + K_{T3} \frac{\dot{x}}{V} + K_{T4} \theta_C ,$$

$$\delta_{E_C} = K_{D1} V_a - K_{D2} \frac{\dot{z}}{V} - K_{D3} \frac{\dot{x}}{V} + K_{D4} \theta_C ,$$

where K_{T1} and K_{D1} are the variable gains calculated from the system Equations (13), (14), and (15) under zero wind conditions, given by

$$\begin{bmatrix} K_{T1} \\ K_{T2} \\ K_{T3} \\ K_{T4} \end{bmatrix} = \begin{bmatrix} G_{10} & G_{11} & -G_{12} \\ D_2 & 0 & 0 \\ 0 & -D_2 & 0 \\ 0 & -1 & 0 \end{bmatrix} \begin{bmatrix} H_9 \\ H_{10} \\ H_{11} \end{bmatrix} ,$$

and

$$\begin{bmatrix} K_{D1} \\ K_{D2} \\ K_{D3} \\ K_{D4} \end{bmatrix} = \begin{bmatrix} -G_{10} & G_{11} & G_{12} \\ -D_2 & 0 & 0 \\ 0 & -D_2 & 0 \\ 0 & -1 & 0 \end{bmatrix} \begin{bmatrix} H_6 \\ H_7 \\ H_8 \end{bmatrix}$$

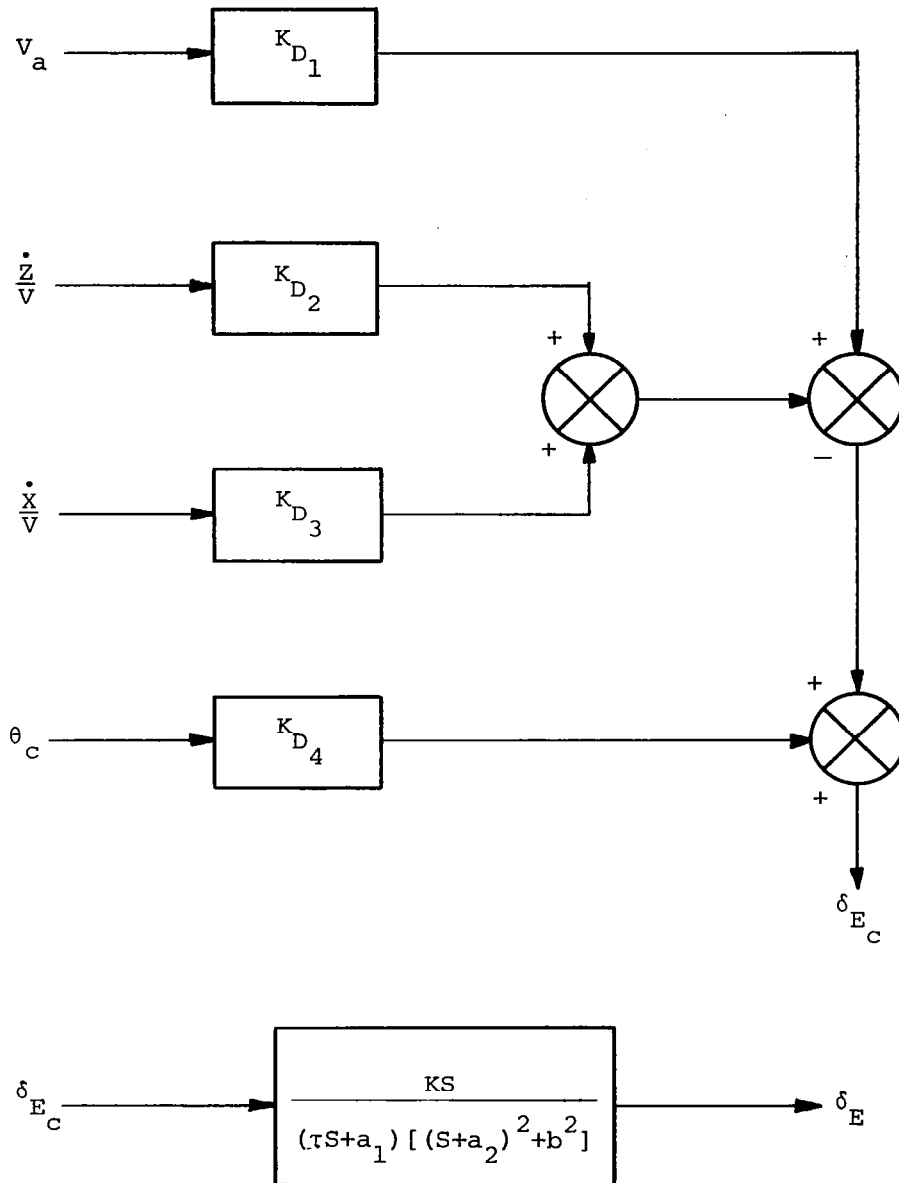


Figure 18 Feedback loop-elevator angle

where

$$G_1 = D_7$$

$$G_2 = - (C_1 + C_2 \alpha) \cos(\gamma' - \gamma) - C_3 \sin(\gamma' - \gamma)$$

$$G_3 = - C_4 \sin(\gamma' - \gamma)$$

$$G_4 = D_6 \cos(\delta_T + \alpha)$$

$$G_5 = C_3 \cos(\gamma' - \gamma) - (C_1 + C_2 \alpha) \sin(\gamma' - \gamma)$$

$$G_6 = C_4 \cos(\gamma' - \gamma)$$

$$G_7 = D_6 \sin(\delta_T + \alpha)$$

$$G_8 = C_5$$

$$G_9 = C_6$$

$$G_{10} = C_7 V_a \cos(\gamma' - \gamma) + (C_8 V_a + C_9 q + C_{10} \dot{\alpha}') \sin(\gamma' - \gamma)$$

$$G_{11} = (C_8 V_a + C_9 q + C_{10} \dot{\alpha}') \cos(\gamma' - \gamma) - C_7 V_a \sin(\gamma' - \gamma)$$

$$G_{12} = C_{11} V_a + C_{12} q + C_{13} \dot{\alpha}'$$

$$H_1 = G_6 G_1 - G_7 G_9$$

$$H_2 = G_5 G_1 - G_7 G_8$$

$$H_3 = G_5 G_9 - G_6 G_8$$

$$H_4 = G_2 H_1 - G_3 H_2 + G_4 H_3$$

$$H_5 = V_a^2 H_4$$

$$H_6 = H_2 / H_5$$

$$H_7 = (G_2 G_1 - G_4 G_8) / H_5$$

$$H_8 = (G_2 G_7 - G_4 G_5) / H_5$$

$$H_9 = H_3 / H_4$$

$$H_{10} = (G_2 G_9 - G_3 G_8) / H_4$$

$$H_{11} = (G_2 G_6 - G_3 G_5) / H_4 ,$$

with the C_n values provided in the appendix.

CHAPTER V

RESULTS AND DISCUSSION

The two-dimensional equations of motion, Equations (1), (2), and (3), for the aircraft discussed in Chapter II were solved on a digital computer using a fourth-order Runge-Kutta technique. Wind models incorporated into the governing equations include (1) atmospheric flow over simulated buildings, (2) atmospheric flow in the absence of buildings, and (3) atmospheric flow associated with thunderstorm gust fronts. The influence of these wind fields on the aircraft landing under different conditions of terrain roughness is investigated. The aircraft characteristics used in the simulation are that of the DC-8 and the DHC-6, specifications of which are given in the Appendix. The initialization conditions for the simulated landings of the aircraft with fixed controls are trimmed conditions on a -2.7 degree glide slope, with the descent beginning at an altitude of 91.4 meters (300 feet). This corresponds to a touchdown point of 1939 meters (6361 feet), down range from where the descent begins. Any variation in winds will cause the aircraft to deviate from the glide slope. The deviation in touchdown point for fixed control conditions is defined as the distance between the actual touchdown point and the intended glide slope touchdown point.

Figures 19 and 20 show the descent trajectories of the aircraft into a wind blowing over a two-dimensional bluff-type body, similar to a block building, and a step, similar to a long, wide building,

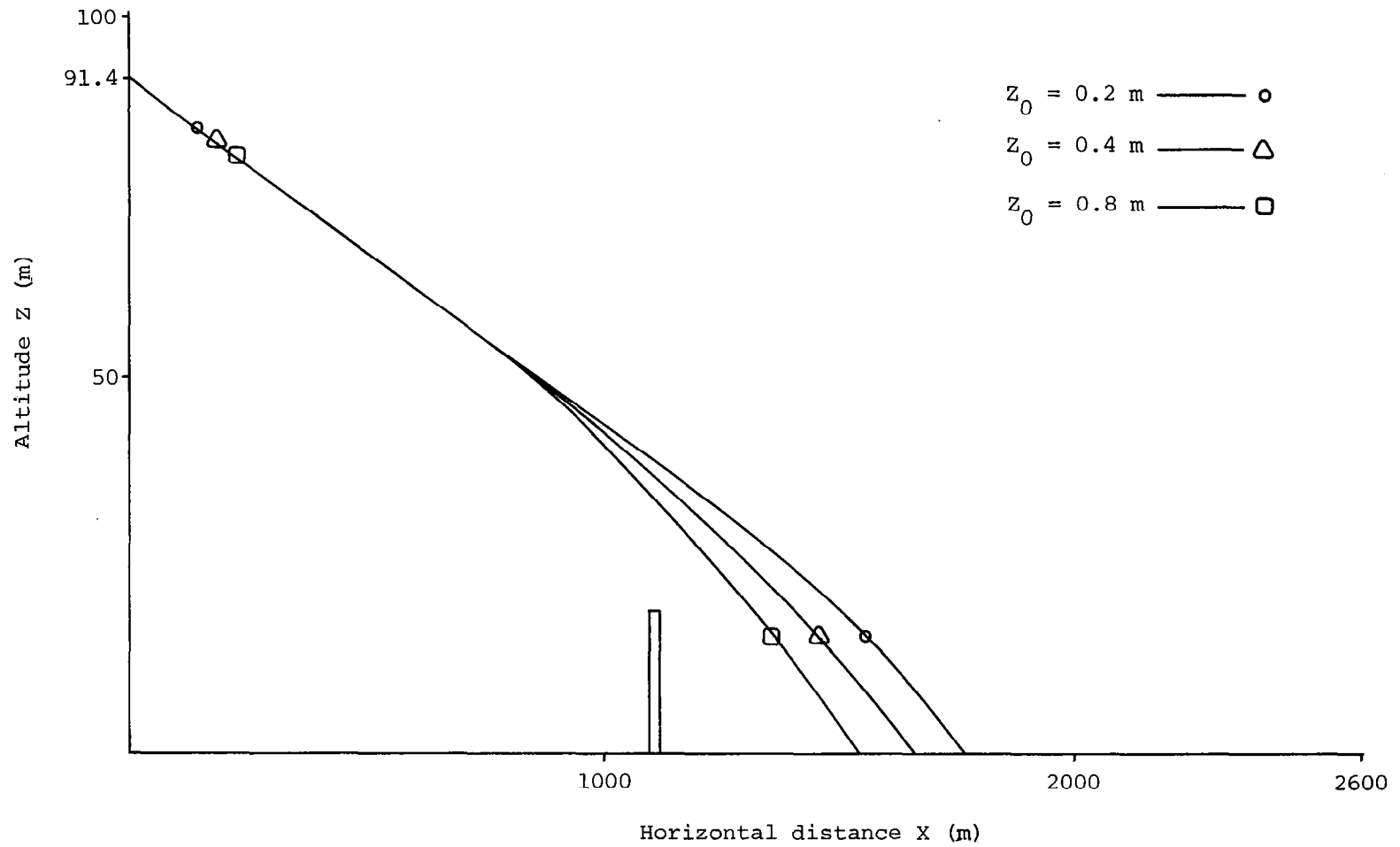


Figure 19 Fixed control landing over a block building

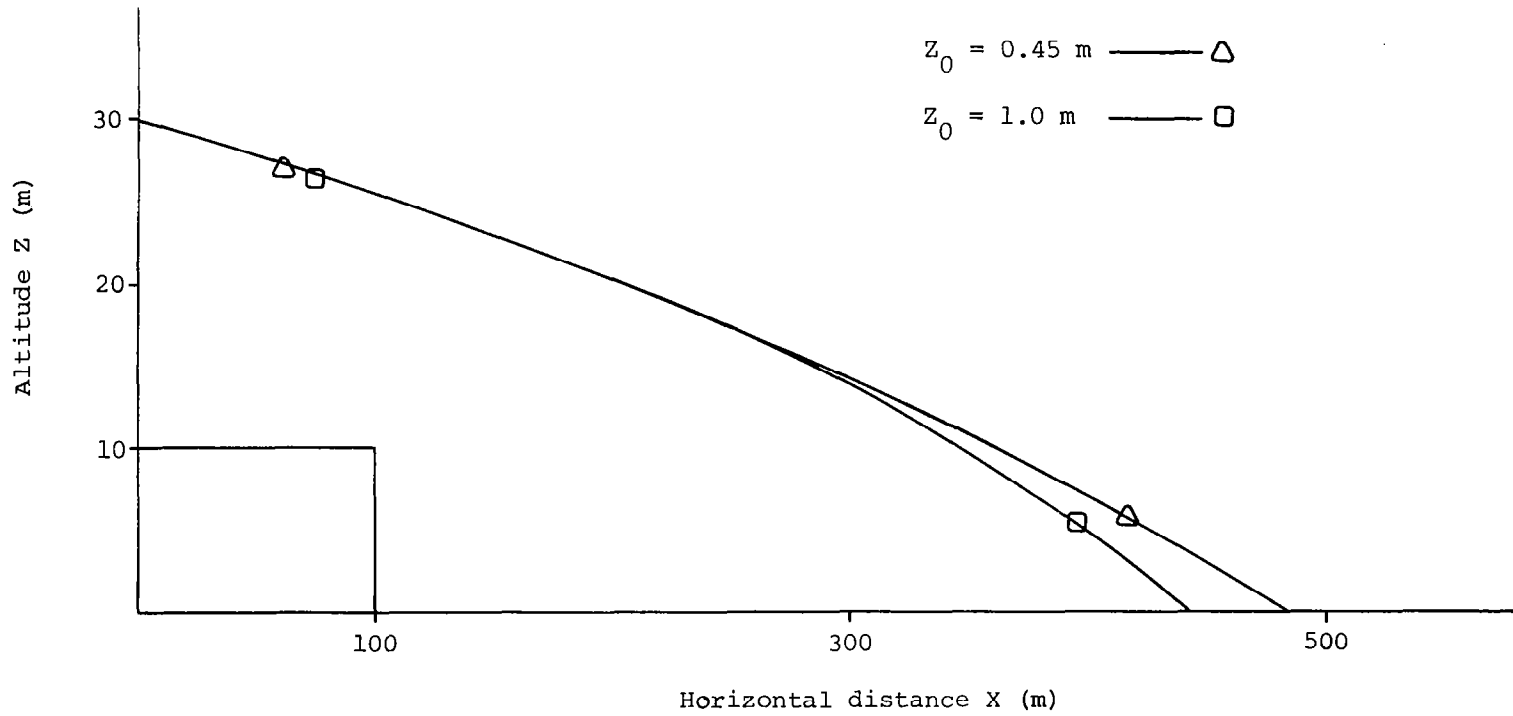


Figure 20 Fixed control landing over a step

respectively. The heights of the simulated block building and the step building are of 20 m and 10 m, respectively. Figure 21 shows the trajectories of the aircraft in identical wind conditions without the presence of the building (i.e., the neutral atmospheric boundary layer), and Figure 22 shows the descent trajectories of the aircraft into the wind fields characteristic of a thunderstorm gust front.

Figures 23 and 24 show the winds, both horizontal and vertical, that were encountered during the descent of the aircraft through the building-disturbed winds--a block building and a long, wide building, respectively. Figure 25 shows the horizontal and vertical winds that were encountered by the aircraft during descent through the thunderstorm gust front. Three flow conditions were used in each simulation of the wind fields for the flow over the block building, for the atmospheric boundary layer flow without the building present, and for the thunderstorm gust front. The surface roughness parameter, Z_0 , was parametrically assigned the values of 0.2, 0.4 and 0.8 m, with corresponding friction velocities, u_* , of 1.25 m/sec, 1.4 m/sec, and 1.6 m/sec, respectively. These combinations of friction velocity and surface roughness give wind speeds of 12.3 m/sec, 11.4 m/sec, and 10.4 m/sec, respectively, at an altitude of 10 meters. For simulation of flow over a long, wide building, surface roughness values of 0.45 meters and 1.0 meters were used, with an assigned wind speed of 10 m/sec at an altitude of 10 meters. This corresponds to friction velocities of 1.27 m/sec and 2.5 m/sec, respectively.

Figures 26, 27, 28 and 29 show the landing trajectories of the aircraft with automatic controls, through the atmospheric boundary

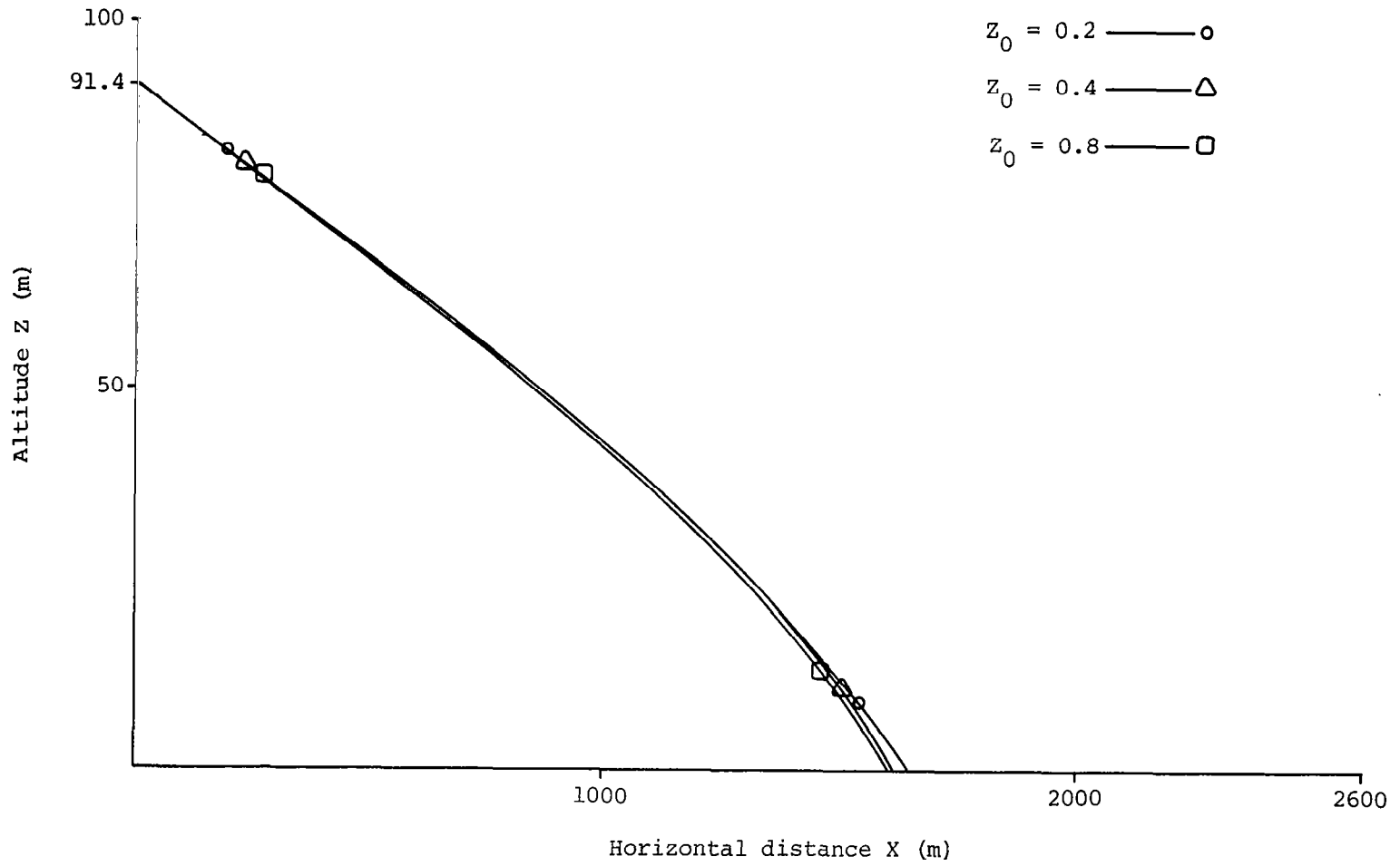


Figure 21 Fixed control landing in the atmospheric boundary layer

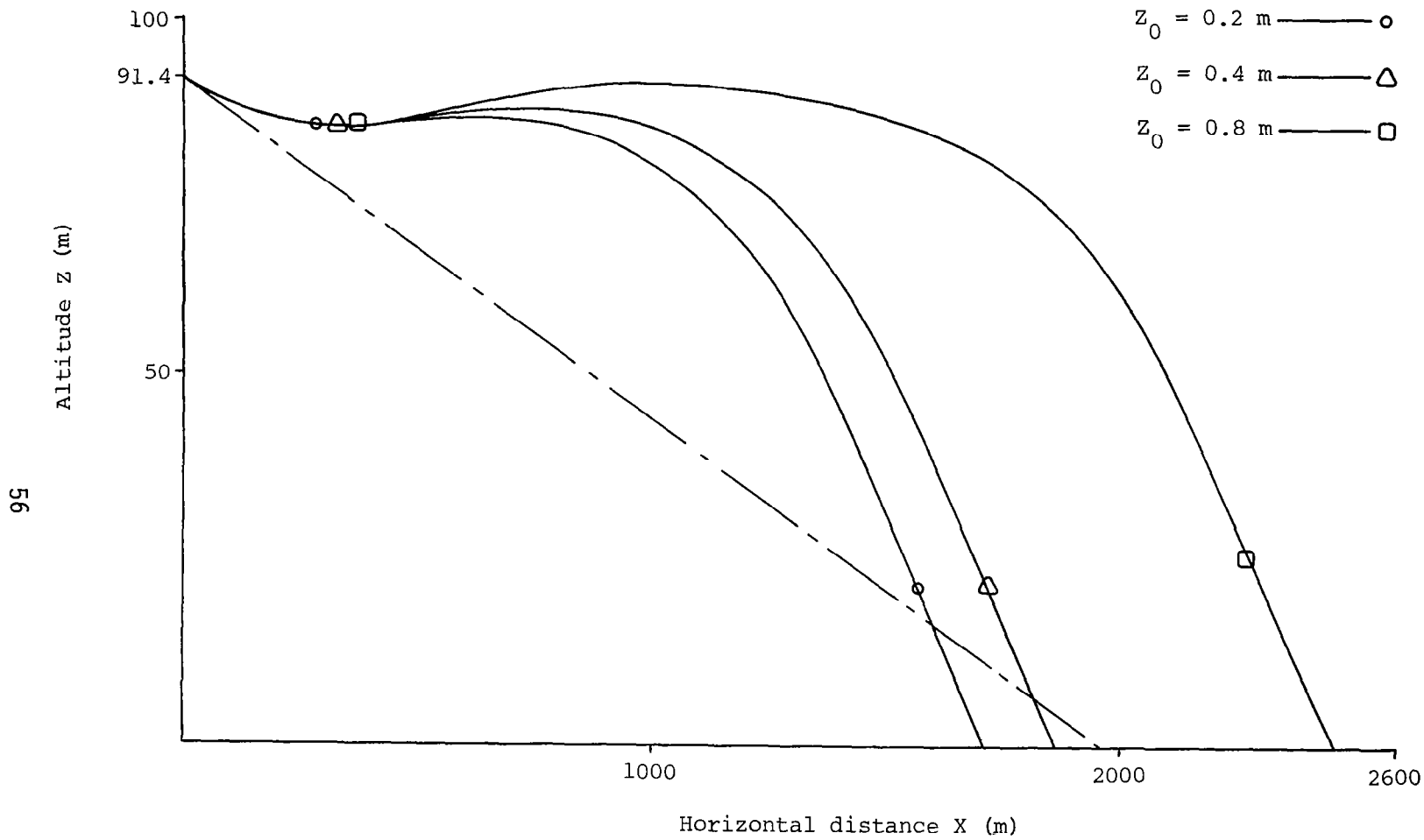


Figure 22 Fixed control landing in thunderstorm gust front

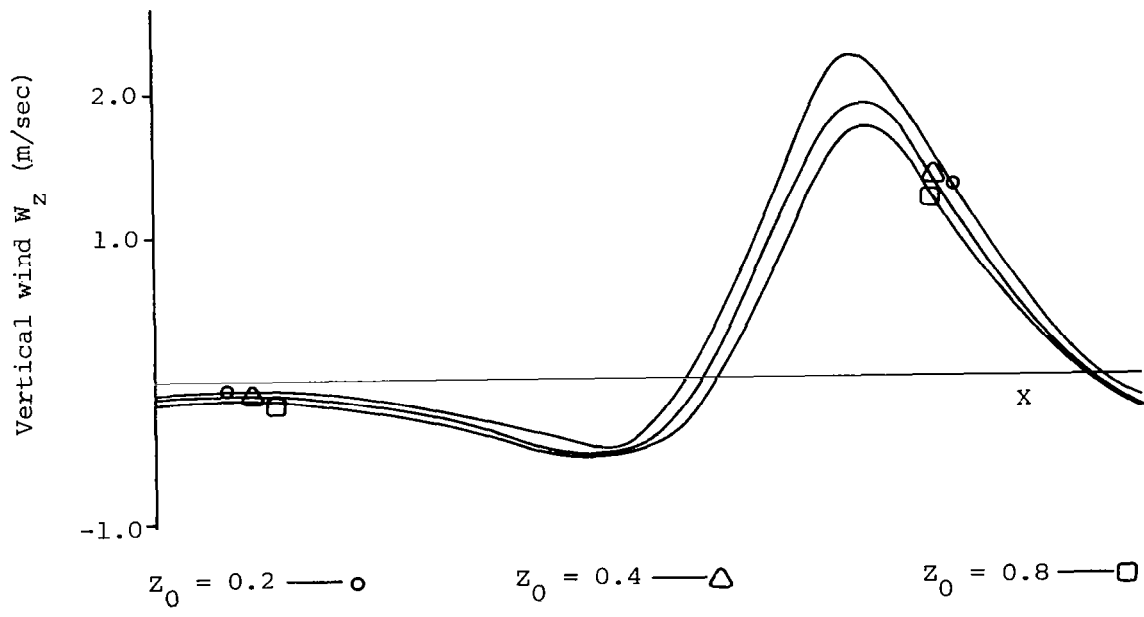
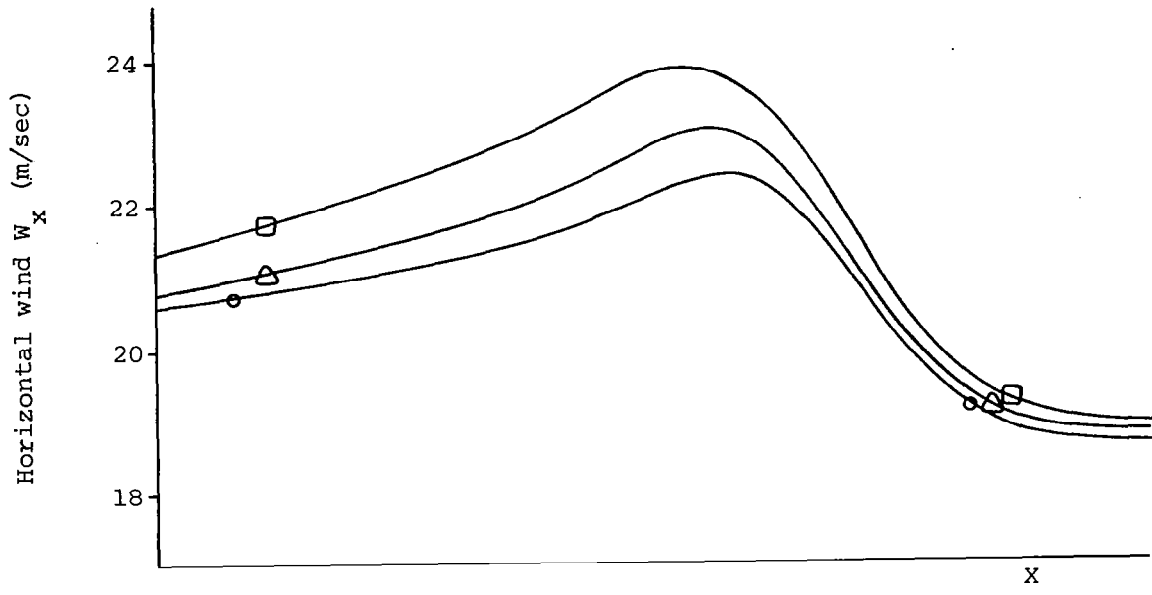


Figure 23 Wind distribution over a block building along the flight path

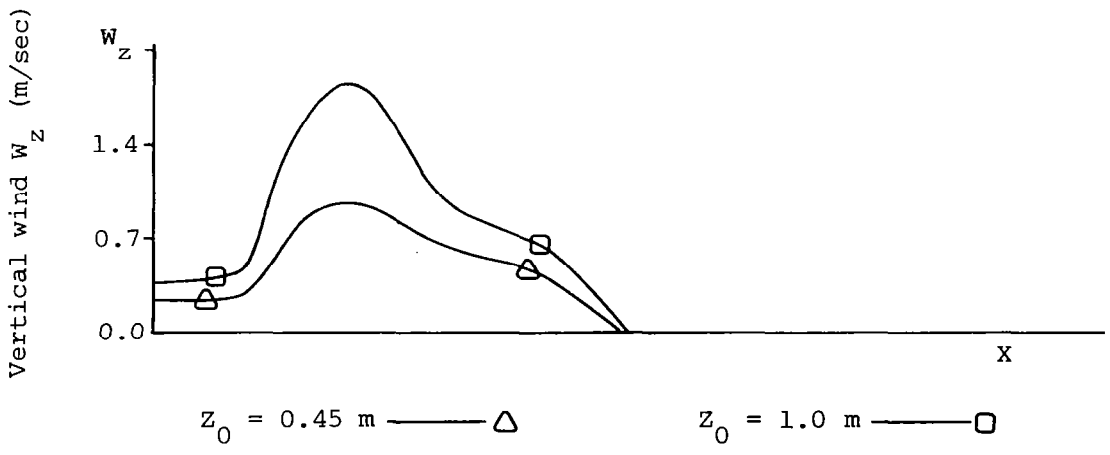
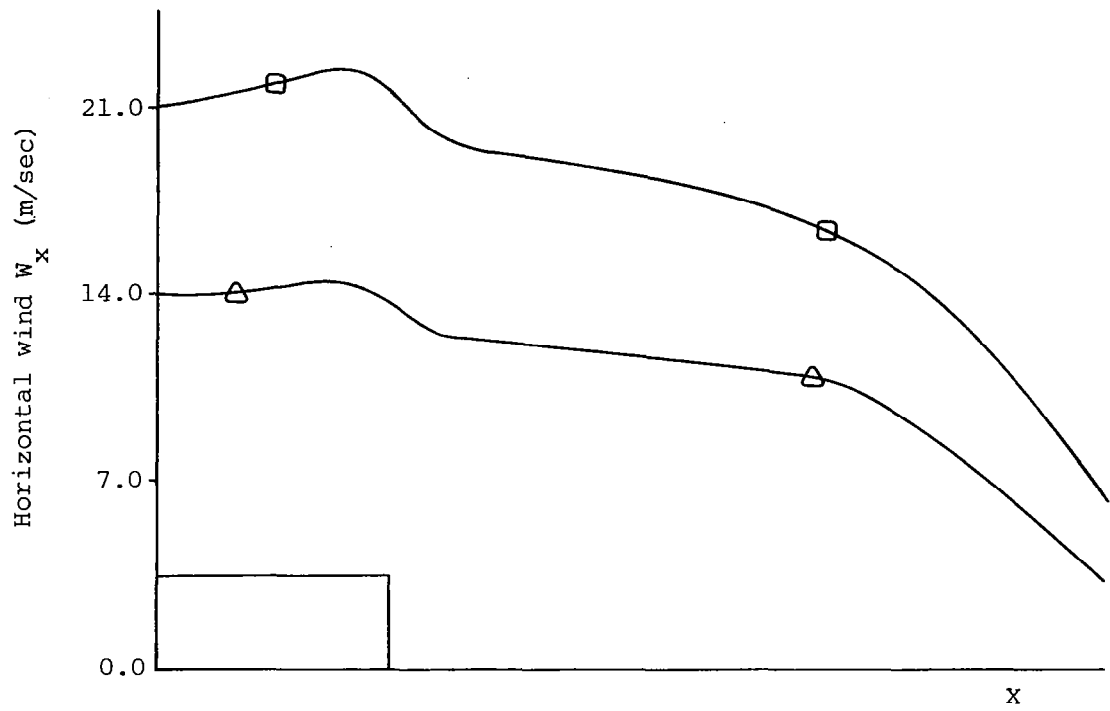


Figure 24 Wind distribution over a long, wide building along the flight path

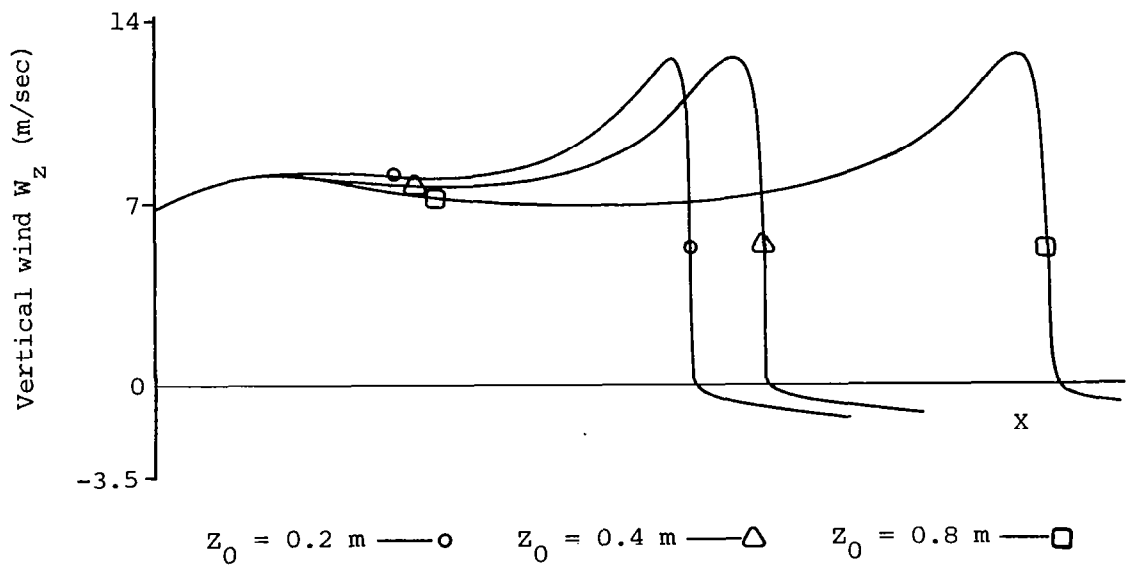
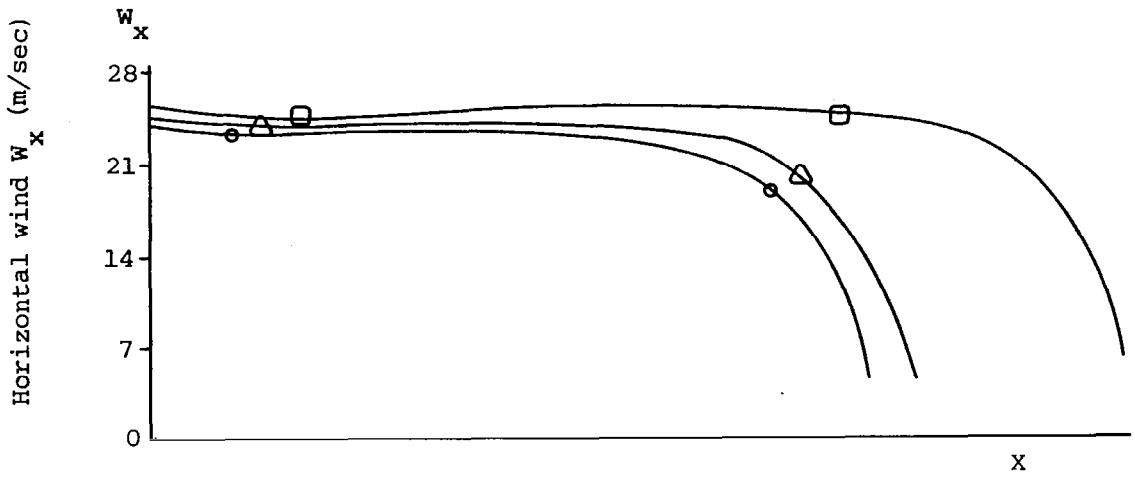


Figure 25 Wind distribution in the thunderstorm gust front along the flight path

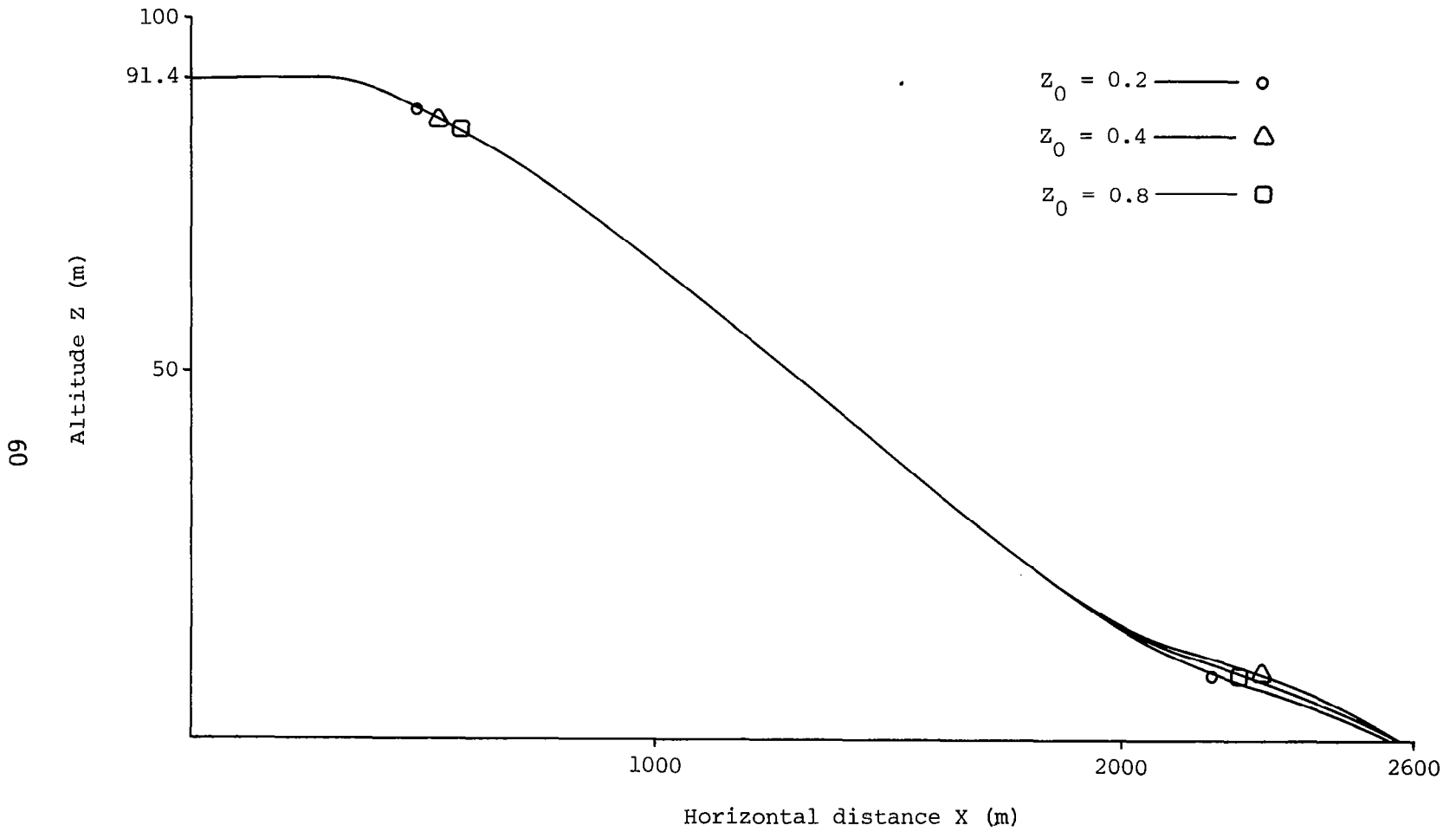


Figure 26 Automatic landing in atmospheric boundary layer

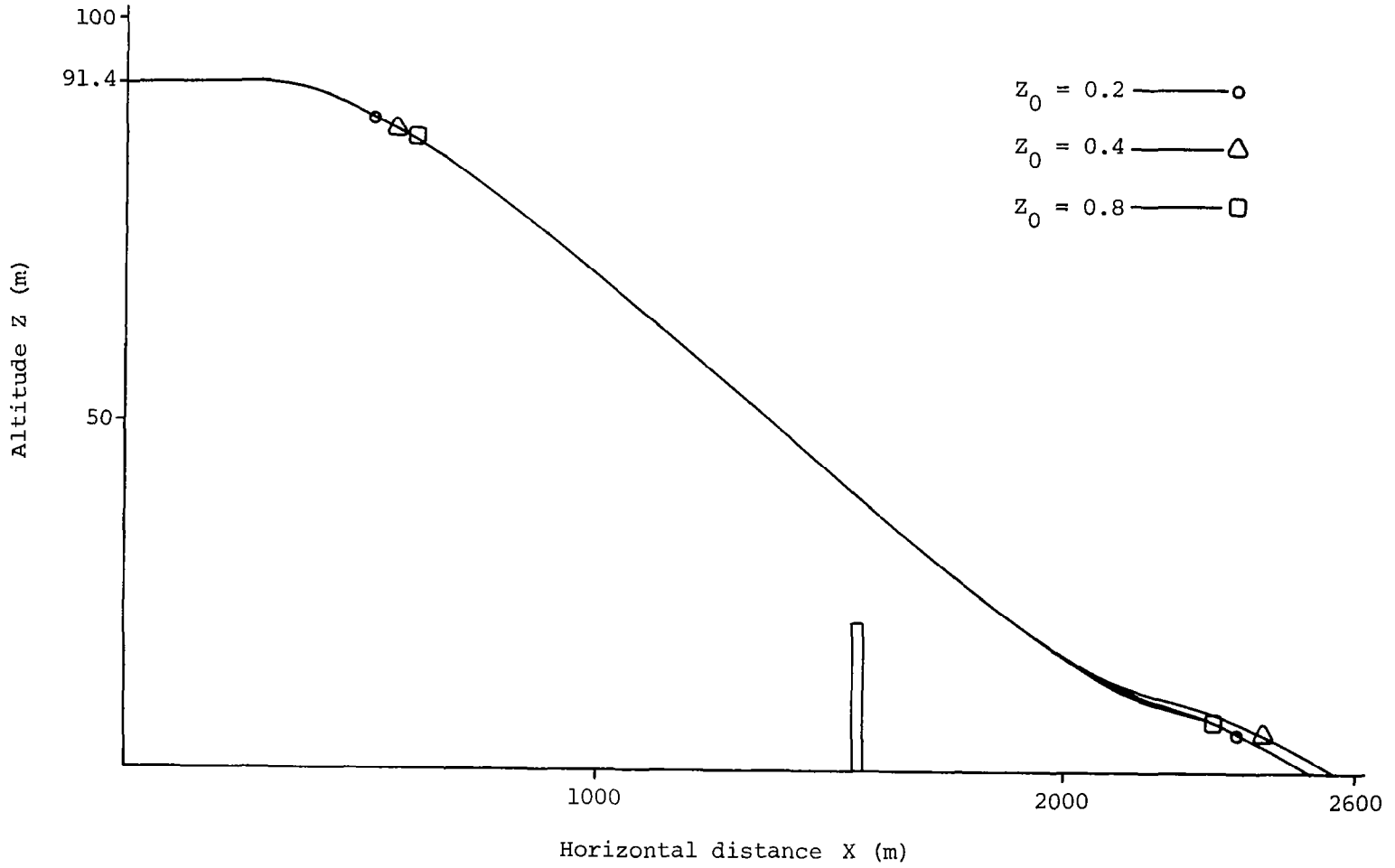


Figure 27 Automatic landing over block building

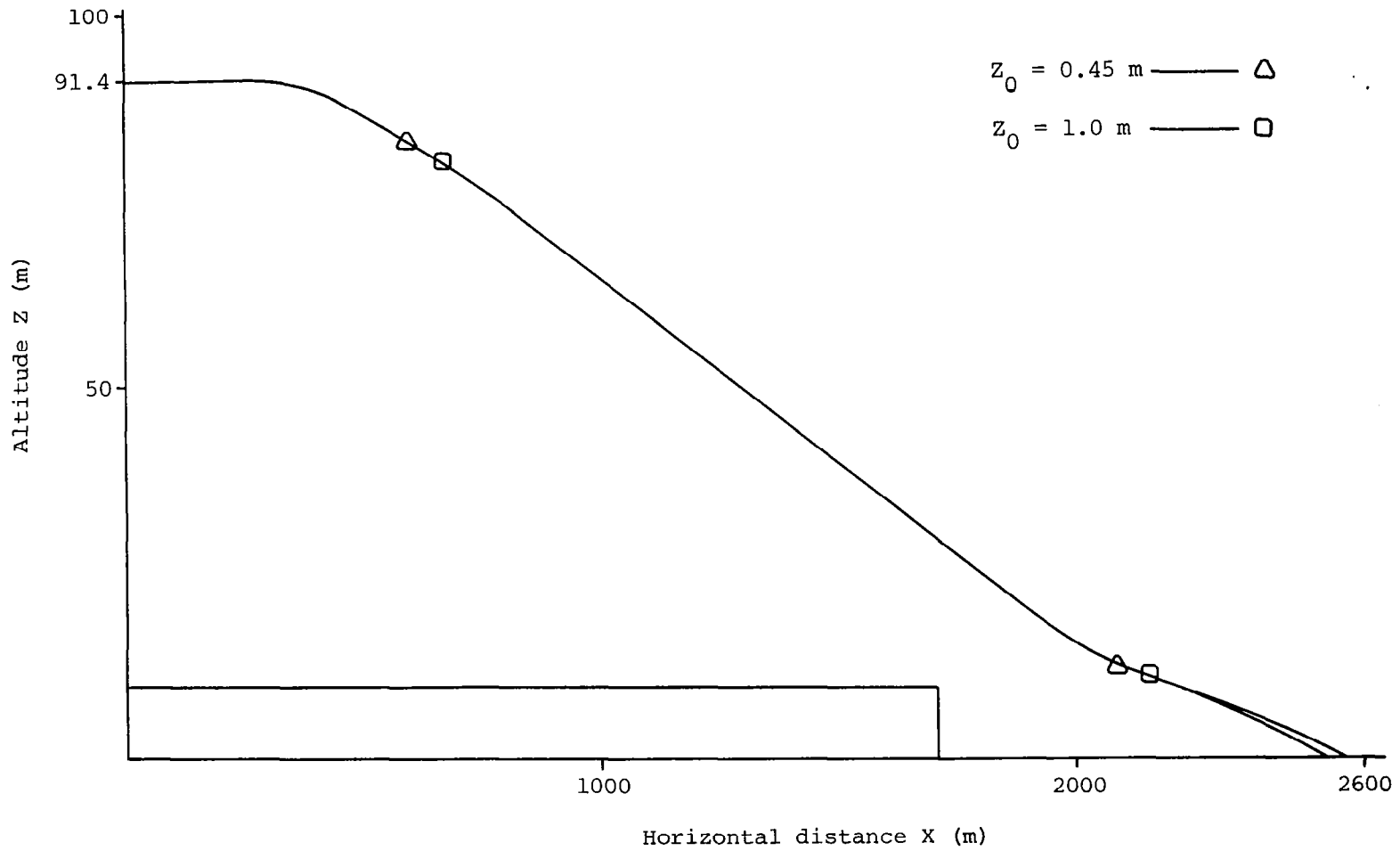


Figure 28 Automatic landing over a long, wide building

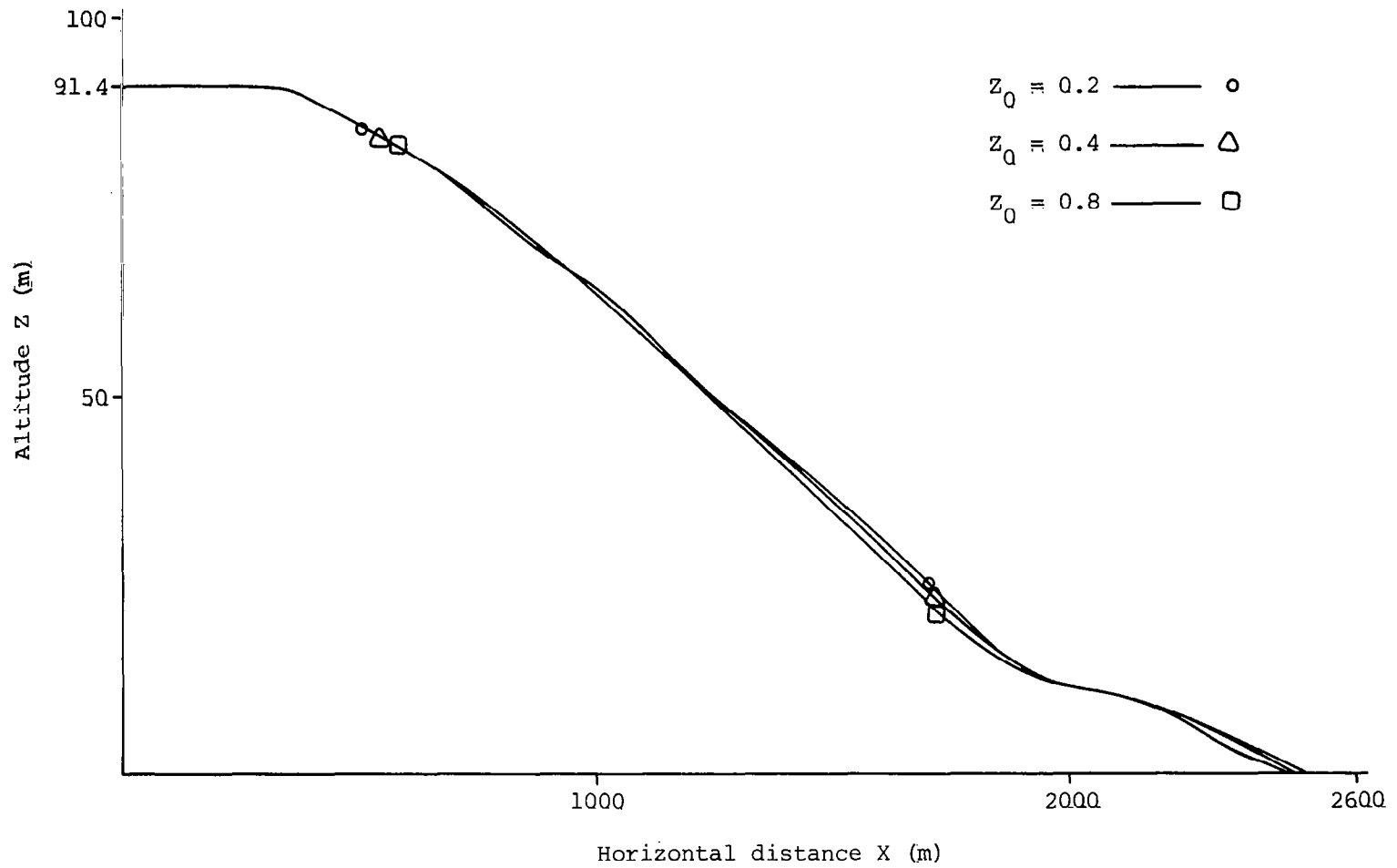


Figure 29 Automatic landing in the flow associated with thunderstorm gust front

layer without the presence of the building, flow over a block building, flow over a long, wide building, and a thunderstorm gust front, respectively. The same wind field simulations that were used in the landing simulation with the fixed controls are applied here also. Figures 30, 31 and 32 show the controls, thrust and elevator angle, that were actuated by the automatic control system to track the glide slope through the block building, the long, wide building, and the thunderstorm gust front disturbed wind fields, respectively. Additionally, Figure 33 shows the trajectory of an aircraft with the characteristics of a DHC-6 Twin Otter with automatic controls landing through the atmospheric flow over a block geometry building.

The deviations from the touchdown point in the different wind fields are presented in Table 1. Note that a positive deviation indicates a long landing and a negative deviation indicates a short landing. The deviation point for the automatically-controlled aircraft was taken as the difference between the actual touchdown point and the touchdown point determined by the prescribed trajectory. This value is computed, as illustrated in Figure 34, by adding $X = 3h_r$, the specified condition for capture to begin, $\Delta X_{cap} = 0.02h_r$ required for the glide slope to be captured, $Z_1 \cot \gamma_0$, the horizontal distance covered while on the glide slope, and $0.2h_r \cot \gamma_f$, the horizontal distance traversed during flare. The value of γ_f is specified as 1.35 degrees.

One observes that the aircraft made short landings in almost all cases with fixed controls. By comparing the landing of the aircraft in the atmospheric boundary layer, with and without the presence of the

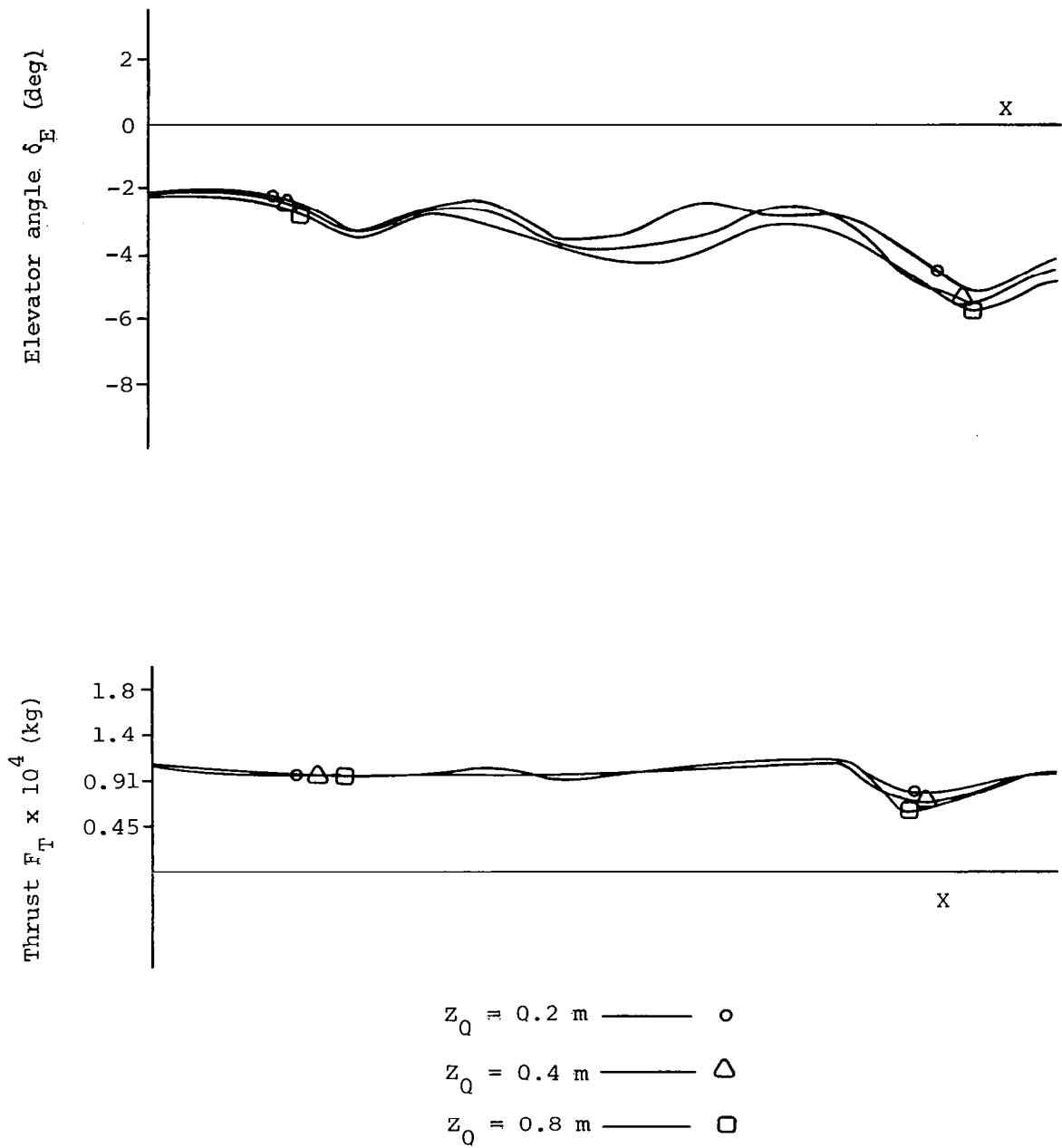


Figure 30 Controls required for landing over a block building

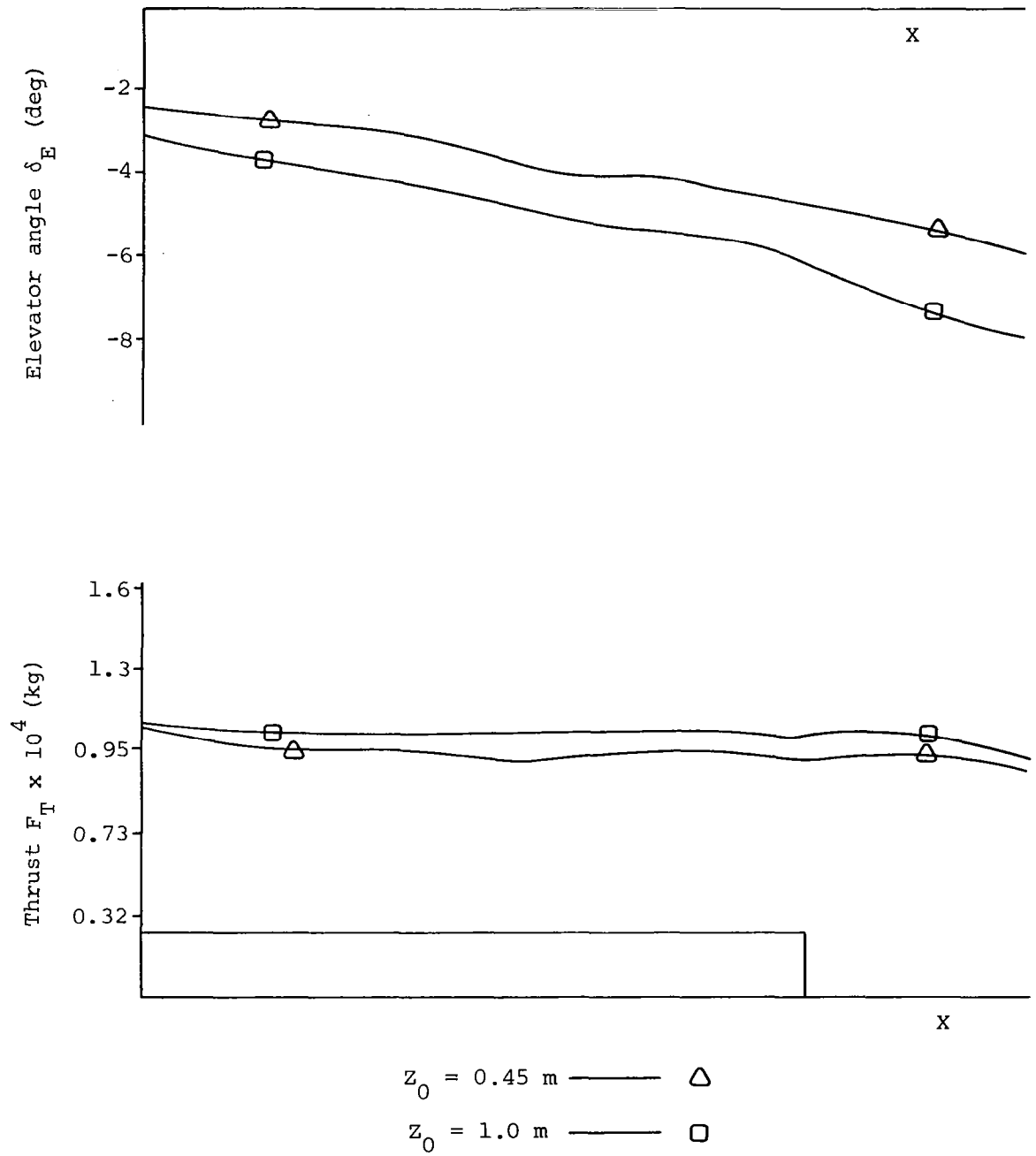


Figure 31 Controls required for landing over a step

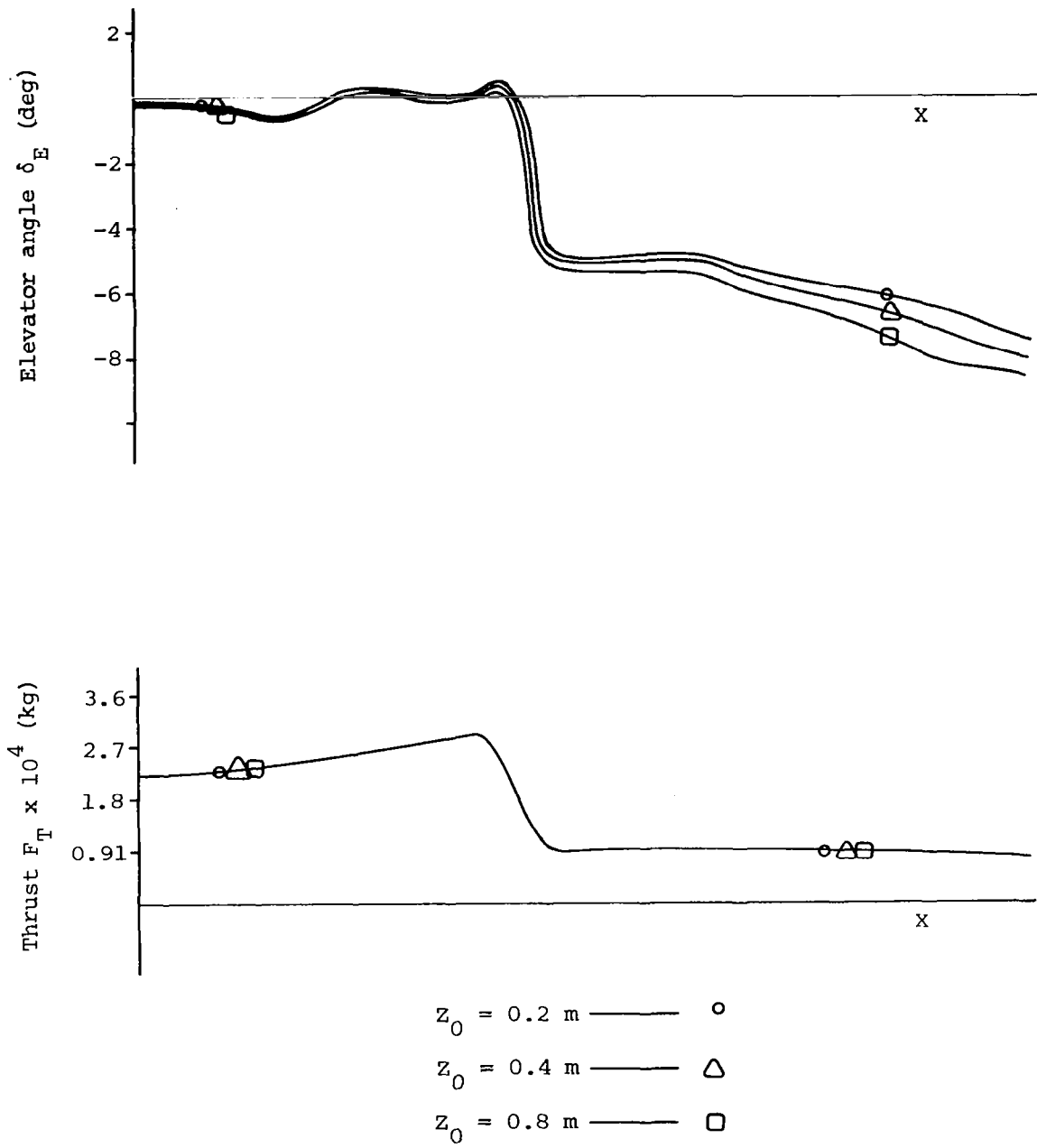


Figure 32 Controls required for automatic landing in thunderstorm gust front

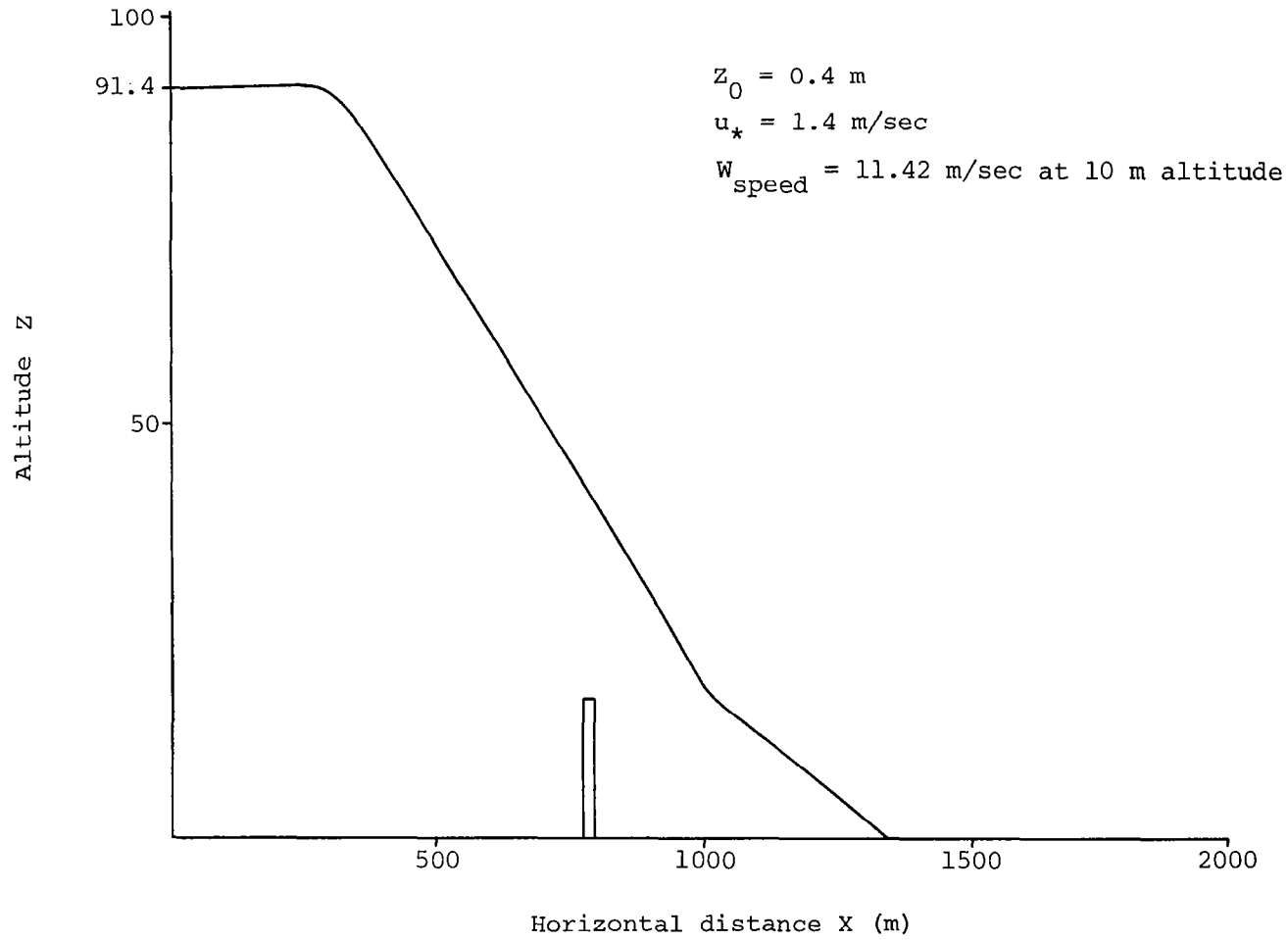


Figure 33 DHC-6 landing through atmospheric flow over a block building

Table 1. Deviation from touchdown point

Wind Condition	With Fixed Controls (meters)	With Automatic Controls (meters)
I. Flow over a building		
(1) Block geometry		
a. $Z_0=0.2\text{m}$ $u_* = 1.25\text{m/sec}$	-198	+35
b. $Z_0=0.4\text{m}$ $u_* = 1.4\text{ m/sec}$	-309	-30
c. $Z_0=0.8\text{m}$ $u_* = 1.6\text{ m/sec}$	-415	-5
(2) Long step geometry		
a. $Z_0=0.45\text{m}$ $u_* = 1.27\text{m/sec}$	-147	-15
b. $Z_0=1.0\text{m}$ $u_* = 2.5\text{ m/sec}$	-185	+11
II. Flow without building present		
a. $Z_0=0.2\text{m}$ $u_* = 1.25\text{m/sec}$	-313	-14
b. $Z_0=0.4\text{m}$ $u_* = 1.4\text{ m/sec}$	-328	+7
c. $Z_0=0.8\text{m}$ $u_* = 1.6\text{ m/sec}$	-350	+6
III. Flow associated with thunderstorm gust fronts		
a. $Z_0=0.2\text{m}$ $u_* = 1.25\text{m/sec}$	-223	+19
b. $Z_0=0.4\text{m}$ $u_* = 1.4\text{ m/sec}$	-80	+8
c. $Z_0=0.8\text{m}$ $u_* = 1.6\text{ m/sec}$	+505	-27

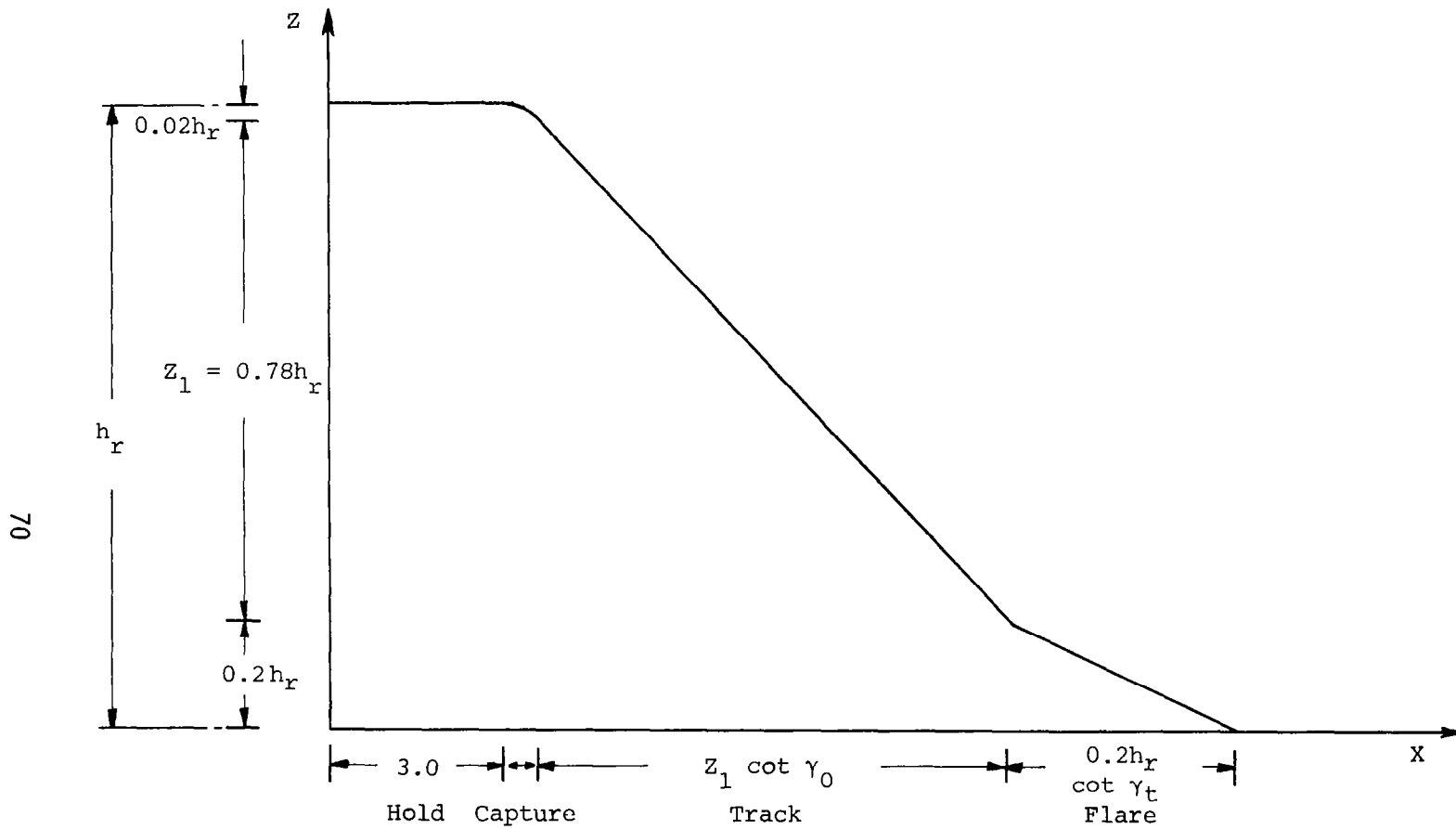


Figure 34 Automatic landing reference trajectory

building, one can observe the effect of complex wind patterns caused by the presence of the large bluff objects. The aircraft lands approximately 300 meters short of the touchdown point in the atmospheric flow without the building, which is a direct result of the decreasing head wind with elevation. However, this is a predictable effect and all landings are within 37 meters of one another, as shown by Figure 21, page 55. Landing through the same atmospheric flow over buildings, however, causes larger variations in touchdown point between the different wind conditions. With a surface roughness value of 20 cm the aircraft lands approximately 200 meters short, whereas for a Z_0 of 80 cm the aircraft lands approximately 400 meters short.

This variation in touchdown points can be explained by looking at the winds encountered by the aircraft along the flight path; see Figure 23, page 57, and Figure 24, page 58. The aircraft encounters an increased head wind (positive horizontal shear) and a downdraft just before the building. An increasing head wind during approach with fixed controls causes the aircraft to be high on the glide slope. This effect is absent in the undisturbed atmospheric boundary layer because of the continuously decreasing head wind, which causes the aircraft with fixed controls to always be below the glide slope. The aircraft does have a slight downdraft, but this is not sufficient to overcome the head wind influence. Just past the building, there is a sudden drop in horizontal wind and a sudden increase in updraft. This reverses the previous effect and forces the aircraft to go below the glide slope. Thus, competing wind effects occur relative to the

undisturbed wind field case, resulting in an unpredictable deviation from touchdown.

One observes that the magnitude of the positive horizontal (tail wind) shear is largest for the case of $Z_0 = 20$ cm and smallest for the case of $Z_0 = 80$ cm. Thus, landing under the conditions of $Z_0 = 20$ cm and $Z_0 = 40$ cm creates sufficiently high positive horizontal shears and updrafts to force the aircraft higher during part of the approach than the case with no building present, resulting in shorter deviation from touchdown. The case $Z_0 = 80$ cm does not create as large a positive horizontal shear and updraft and the influence of the decreasing head wind and downdraft in the wake of the building produce a shorter touchdown than occurs with the undisturbed wind field.

In the case of landings through the flow over the long building, the aircraft lands 147 m short for the case $Z_0 = 45$ cm and 185 meters short in the case $Z_0 = 100$ cm. One should notice that in this case the descent starts from an altitude of about 33 meters. Therefore, these touchdown points cannot be compared with the touchdowns in the landings through the atmospheric boundary layer without the building.

However, by looking at the winds encountered by the aircraft along the flight path, one can observe the similarity with the block building case. Just as the aircraft passes over the edge of the building, there is a sudden drop in horizontal wind which causes the aircraft to go below the glide slope, and thereby resulting in an unpredictable deviation from touchdown. One can observe that the difference between the case of $Z_0 = 100$ cm and $Z_0 = 45$ cm is that the

initial head wind is higher and decreases more rapidly. Also, the aircraft encounters a smaller updraft than in the former case which tends to decrease the sink rate. Both of these wind effects result in a shorter touchdown, as indicated by the results in Table 1, page 69.

In the case of landings with automatic controls, the deviations from the touchdown points are very small for landings through the atmospheric flow without the building, as well as with buildings present. Even though the deviations from the touchdown point are not significant, one can see that complex wind patterns created by the presence of large buildings do create larger deviations in touchdown. Moreover, a significant factor on the safety of aircraft operations is the rate at which the controls must be operated to track the glide path. Figure 30, page 65, shows that the thrust must be reduced significantly as the aircraft passes over the building to compensate for the sudden excursions in the horizontal and vertical winds. Thrust was cut almost 50% in the case for $Z_0 = 80$ cm. Figure 31, page 66, shows the controls that were used in the case of flight over the long, wide building. In this case the elevator angle changes quite rapidly to compensate for the effects of changing winds.

Figure 22, page 56, and Figure 29, page 63, show the aircraft landing trajectories in the flow associated with a thunderstorm gust front with fixed controls and with automatic controls, respectively. In the case of fixed control landings, the deviations between touchdown points are large, as much as 725 meters variation from the case for $Z_0 = 20$ cm and for $Z_0 = 80$ cm. Figure 22 shows that there are

very large deviations from the flight path itself and thus would result in unsatisfactory landings.

Figure 25, page 59, shows the winds encountered by the aircraft along the trajectory. Initially, there is high vertical updraft which increases to approximately 13 m/sec and then suddenly drops to almost zero. Thus, the aircraft is initially blown above the glide slope and then suddenly this wind dies out, resulting in a high sink rate. In the case for $Z_0 = 20$ cm, the head wind remains almost constant and then starts decreasing very rapidly; at the same time the vertical updraft suddenly drops to zero, creating a strong turning moment on the aircraft which results in a shorter landing. For landing under the conditions of $Z_0 = 80$ cm, head wind and vertical updraft remain constant for a longer period of time, thus keeping the aircraft above the glide path for a longer period of time.

In the case of landings with automatic controls through this wind field, the deviations from the flight path are small, but the influence of these severe winds is to cause rapid changes in the controls. Figure 32, page 67, shows the controls that were applied to maintain the flight path. Here thrust starts out initially at a high magnitude, increases slightly and then drops very suddenly to almost one-third of the initial value. This is because the pitch angle is maintained constant in automatic landings, a vertical updraft causes a larger angle of attack and increased drag. Therefore, when the vertical updraft suddenly goes to zero, the angle of attack decreases and drag drops, hence thrust is reduced to prevent going high on the

glide slope. The elevator angle also changes very rapidly from 0 to -6 degrees in the process to compensate for the sudden drop in vertical wind and counterclockwise moment produced by the vertical wind, since a negative elevator setting corresponds to a counterclockwise rotation with the airplane traveling in positive x-direction.

Figure 33, page 68, shows that the aircraft with the characteristics of a DHC-6 on a 6-degree glide path behaves basically the same as a DC-8. For the landing of this aircraft, few changes were required in the automatic control system. In the glide-slope capture mode the reference flight path angle was changed from 2.7 to 6 degrees and the gain constant, k_3 , from 0.05 to 0.1. In the glide-slope tracking mode the constant, a_3 , is changed from 0.01 to 0.02, and in the flare mode the constant, a_6 , is changed from 4.0 to 5.0. These changes in different control modes increase the response of pitch angle command variable, θ_c .

CHAPTER VI

CONCLUSIONS

The two-dimensional aircraft landing simulation study has provided some basic results concerning the problems of wind shear due to the presence of large buildings or other bluff geometries. The aircraft encountering a strong wind shear caused by the edge of a building is drawn towards the building. With fixed controls, deviation in touchdown point in excess of 400 m resulting from variation of the horizontal wind during the final 100 m of descent has been computed under wind shear conditions that may realistically be encountered around buildings or bluff terrain features.

Wind shear due to thunderstorm gust fronts can cause very severe departures from the glide slope during landing. Although thunderstorm gust fronts are not encountered too frequently, landing through such a gust front can be very hazardous and requires rapid changes in the controls required to maintain the flight path. Based on the model of thunderstorm field investigated in this report, changes in the controls at the rate of 7 degrees of elevator angle and 9072 kg of thrust per one-half second for the DC-8 were required.

Although the surface roughness parameter, Z_0 , shows little influence on touchdown points during the landings through the atmospheric flow over level terrains, it does have considerable effect on aircraft landing when large buildings or bluff objects are present near the airports.

BIBLIOGRAPHY

1. Etkin, B., Dynamics of Atmospheric Flight. John Wiley & Sons, Inc., New York, 1972.
2. Blakelock, John H., Automatic Control of Aircraft and Missiles. John Wiley & Sons, Inc., New York, 1965.
3. Neuman, F., and J. Foster, "Investigation of a Digital Automatic Aircraft Landing System in Turbulence," NASA TN D-6066, October, 1970.
4. Melvin, W. W., "Wind Shear on the Approach," Shell Aviation News, 393:16-21, (1971).
5. Kraus, K., "Aspects of the Influence of Low-Level Wind Shear on Aviation Operations," International Conference on Aerospace and Aeronautical Meteorology, Washington, D. C., May 22-26, 1972.
6. Camp, D. W., W. Frost, and W. A. Crosby, "Flight Through Thunderstorm Outflows," to be presented at 11th International Congress of ICAS, Lisbon, Portugal, September 10-16, 1978.
7. Luers, J. K., and J. B. Reeves, "Effect of Shear on Aircraft Landing," National Aeronautics and Space Administration CR-2287, George C. Marshall Space Flight Center, Huntsville, Alabama, July, 1973.
8. National Transportation Safety Board, "Eastern Airlines, Inc., Boeing 727-225, John F. Kennedy International Airport, Jamaica, New York, June 24, 1975," Aircraft Accident Report No. NTSB-AAR-76-8, National Transportation Safety Board, Washington, D. C., March 12, 1976.
9. National Transportation Safety Board, "Iberia Lineas Aereas de Espana (Iberian Airlines), McDonnell Douglas DC-10-30, EC CBN, Logan International Airport, Boston, Massachusetts, December 17, 1973," Aircraft Accident Report No. NTSB-AAR-74-14, National Transportation Safety Board, Washington, D. C., November 8, 1974.

10. Frost, W., and D. W. Camp, "Wind Shear Modeling for Aircraft Hazard Definition." Interim report No. FAA-RD-77-36 prepared for U. S. Department of Transportation, Federal Aviation Administration, Systems Research and Development Service, by FWG Associates, Inc., Tullahoma, Tennessee, March, 1977.
11. Haskins, G. L., "The X in WX," Aerospace Safety, April, 1969.
12. Frost, Walter, "Flight in Variable Mean Winds," Report in preparation for NASA Contract No. NAS8-29584.
13. Gera, J., "The Influence of Vertical Wind Gradients on the Longitudinal Motion of Airplanes," NASA TN D-6430, September, 1971.
14. Johnson, W. A., and D. T. McRuer, "A System Model for Low-Level Approach," Journal of Aircraft, December, 1971.
15. Farrell, J. L., Integrated Aircraft Navigation. Academic Press, New York, 1976.
16. Bosman, D., "Aircraft Flight Instrumentation Integrated Data Systems," AGARD Conference Proceedings Number Six, November, 1967.
17. Tanney, J. W., "Fluidics," Progress in Aeronautical Sciences, Volume 10. Pergamon Press, Oxford, 1970.
18. Blackadar, A. K., "The Vertical Distribution of Wind and Turbulent Exchange in a Neutral Atmosphere," Journal of Geophysical Research, 67:3095-3102, April, 1962.
19. Lettau, H. H., "Wind Profile, Shear Stress and Geostrophic Drag Coefficients in the Atmospheric Surface Layer," Advances in Geophysics. Academic Press, New York, 1962.
20. Frost, W., J. R. Maus, and W. R. Simpson, "A Boundary Layer Approach to the Analysis of Atmospheric Motion Over a Surface Obstruction," NASA CR-2182, January, 1973.
21. Panofsky, H. A., "The Atmospheric Boundary Layer Below 150 Meters," Annual Review of Fluid Mechanics, Vol. 6, 1974.
22. Shieh, C. F., W. Frost, and J. Bitte, "Neutrally Stable Atmospheric Flow Over a Two-Dimensional Rectangular Block," Report prepared under NASA Contract No. NAS8-29584, The University of Tennessee Space Institute, Tullahoma, Tennessee, December, 1976.

23. Bitte, J., and W. Frost, "Atmospheric Flow Over Two-Dimensional Bluff Surface Obstructions," NASA CR-2750, October, 1976.
24. Johnson, W. A., and D. T. McReur, "Development of a Category II Approach System Model," Technical Report 182-1, Systems Technology, Inc., December, 1969.
25. Osder, S. S., "Avionics Requirements for All Weather Landing of Advanced SST's," Volume I, NASA CR-73092, 1967.
26. Fichtl, G. H., and D. W. Camp, Memo to Mr. Frank Coons, ARD 451, FAA, 2100 2nd Street, S. W., Washington, D. C., 20590, March 22, 1976.
27. Goff, R. C., "Thunderstorm Outflow Kinematics and Dynamics," NOAA Technical Memo ERL NSSL-75 (1975).

APPENDIX

APPENDIX

The aircraft characteristics used in this simulation study are for that of a DC-8 and a DHC-6. The initial conditions and aircraft physical data are given as follows [7]:

	<u>DESCRIPTION</u>	<u>DC-8</u>	<u>DHC-6</u>
H(m)	Reference altitude	91	91
V_a (m/sec)	Initial velocity	70	46
γ (deg)	Initial flight path angle	-2.7	-6.0
W(kg)	Aircraft weight	90700	4985
I_{yy} (kg-m ²)	Moment of inertia	5.3×10^6	3.2×10^4
L_T (m)	Moment arm of thrust vector	1.2	-0.91
δ_T (deg)	Angle between F_T and FRL	3.15	0.0
\bar{c} (m)	Chord length	7	2
s (m ²)	Wing area	256	39

The expressions for the aerodynamic coefficients of the DC-8 aircraft are:

$$C_L = C_{L_0} + C_{L_\alpha} \alpha' + C_{L_{\delta_E}} \delta_E + \frac{\bar{c}q}{2V_a} C_{L_q} + \frac{\bar{c}\dot{\alpha}'}{2V_a} C_{L_{\dot{\alpha}'}} ,$$

$$C_D = C_{D_0} + C_{D_\alpha} \alpha' + C_{D_{\alpha^2}} \alpha'^2 ,$$

$$C_m = C_{m_0} + C_{m_\alpha} \alpha' + C_{m_{\delta_E}} \delta_E + \frac{\bar{c}q}{2V_a} C_{m_q} + \frac{\bar{c}\dot{\alpha}'}{2V_a} C_{m_{\dot{\alpha}'}} ,$$

where the usual notation is used for the various stability derivatives.

The values of the stability derivatives are given as follows:

	<u>DC-8</u>	<u>DHC-6</u>
C_{L_0}	0.90	0.86
C_{L_α}	5.30/rad	6.109/rad
$C_{L_{\delta_E}}$	0.0053/deg	0.5236/deg
C_{L_q}	7.68/rad	2.152/rad
$C_{L_{\dot{\alpha}}}$	0.0	0.0
C_{D_0}	0.140	0.32
C_{D_α}	0.501/rad	0.9832/rad
$C_{D_{\alpha^2}}$	1.818/rad ²	0.0
C_{m_0}	-1.01	0.0/rad ²
C_{m_α}	-1.062/rad	-2.026/rad
$C_{m_{\delta_E}}$	-0.0161/deg	-2.068/deg
C_{m_q}	-12.30/rad	-28.76/rad
$C_{m_{\dot{\alpha}}}$	-4.01/rad	-8.663/rad

The various dimensionless groups (normalizing factors) used in this study are provided below:

$$D_1 = \frac{\rho}{2} \frac{SH}{w}$$

$$D_2 = \frac{gH}{V_a^2}$$

$$D_3 = \frac{H^2}{V_a^2}$$

$$D_4 = \frac{\bar{c}}{2H}$$

$$D_5 = \frac{\rho}{2} \frac{s\bar{c}H^2}{g I_{yy}}$$

$$D_6 = \frac{gH}{w V_a^2}$$

$$D_7 = \frac{L_T D_3}{I_{yy}}$$

The following are the "C" coefficients used in variable gain computations of

F_{TC} and δ_{EC} :

$$C_1 = D_1 C_{D_\alpha}$$

$$C_2 = D_1 C_{D_\alpha^2}$$

$$C_3 = D_1 C_{L_\alpha}$$

$$C_4 = D_1 C_{L_{\delta_E}}$$

$$C_5 = D_5 C_{m_\alpha}$$

$$C_6 = D_5 C_{m_{\delta_E}}$$

$$C_7 = D_1 C_{D_0}$$

$$C_8 = D_1 C_{L_0}$$

$$C_9 = D_1 D_4 C_{L_q}$$

$$C_{10} = D_1 D_4 C_{L\alpha}$$

$$C_{11} = D_5 C_{m_0}$$

$$C_{12} = D_5 D_4 C_{m_q}$$

$$C_{13} = D_5 D_4 C_{m\alpha}$$

1. REPORT NO. NASA CR-3073	2. GOVERNMENT ACCESSION NO.	3. RECIPIENT'S CATALOG NO.	
4. TITLE AND SUBTITLE Investigation of Aircraft Landing in Variable Wind Fields		5. REPORT DATE December 1978	6. PERFORMING ORGANIZATION CODE
		8. PERFORMING ORGANIZATION REPORT #	
7. AUTHOR(S) Walter Frost and Kapuluru Ravikumar Reddy		10. WORK UNIT, NO. M-272	11. CONTRACT OR GRANT NO. NAS8-29584
9. PERFORMING ORGANIZATION NAME AND ADDRESS The University of Tennessee Space Institute Tullahoma, Tennessee		13. TYPE OF REPORT & PERIOD COVERED Contractor	
		14. SPONSORING AGENCY CODE	
12. SPONSORING AGENCY NAME AND ADDRESS National Aeronautics and Space Administration Washington, D. C. 20546		15. SUPPLEMENTARY NOTES Prepared under the technical monitorship of the Atmospheric Sciences Division, Space Sciences Laboratory, Science and Engineering, NASA/Marshall Space Flight Center	
16. ABSTRACT <p>This report describes a digital simulation study of the effects of gusts and wind shear on the approach and landing of aircraft. The gusts and wind shear are primarily those associated with wind fields created by surface wind passing around bluff geometries characteristic of buildings. Also, flight through a simple model of a thunderstorm is investigated.</p> <p>A two-dimensional model of aircraft motion was represented by a set of nonlinear equations which accounts for both spatial and temporal variations of winds. The landings of aircraft with the characteristics of a DC-8 and a DHC-6 are digitally simulated under different wind conditions with fixed and automatic controls. The resulting deviations in touchdown points and the controls that are required to maintain the desired flight path are presented. The presence of large bluff objects, such as buildings in the flight path is shown to have considerable effect on aircraft landings.</p>			
17. KEY WORDS Aviation Safety Aircraft Motion Simulation Low-Level Wind Wind Shear Turbulence		18. DISTRIBUTION STATEMENT Category 47	
19. SECURITY CLASSIF. (of this report) Unclassified	20. SECURITY CLASSIF. (of this page) Unclassified	21. NO. OF PAGES 91	22. PRICE \$6.00